ENGINEERING ATOMICALLY THIN MECHANICAL SYSTEMS

A Dissertation

Presented to the Faculty of the Graduate School

of Cornell University

in Partial Fulfillment of the Requirements for the Degree of

Doctor of Philosophy

by

Robert Anthony Barton, Jr.

January 2013

ENGINEERING ATOMICALLY THIN MECHANICAL SYSTEMS

Robert Anthony Barton, Jr., Ph.D.

Cornell University 2013

Atomically thin materials, which were discovered in 2004 with the isolation of graphene, represent a unique new building block for mechanical systems. Here, we explore the possibilities for a new class of mechanical devices based on these materials, with a focus on graphene-based resonant nanoelectromechanical systems. As a result of the recent progress in fabricating large-area graphene sheets, graphene-based mechanical devices have become vastly easier to manufacture and now show even greater promise for a range of applications, such as signal processing, sensing, and mechanical systems in the quantum regime. We discuss recent advances in fabrication and measurement techniques that make graphene resonators a viable technology, and present what is known about the performance of graphene mechanical systems. We demonstrate in the area of performance that room temperature graphene quality factor can be enhanced an order of magnitude by using a fully-clamped circular geometry with large diameter. We also show that the quality factor of a graphene resonator depends on its tension, and we suggest ways of enhancing the tension in graphene resonators. Finally, we simultaneously utilize graphene's electrical, mechanical, and optical properties in a novel application of graphene: photothermal graphene optomechanics. As a demonstration of the utility of this effect, we show that a continuous wave laser can be used to cool a graphene vibrational mode or to power a graphene-based tunable-frequency oscil-

lator. By virtue of graphene's high thermal conductivity and optical absorption, photothermal optomechanics is efficient in graphene and could ultimately enable laser cooling of graphene mechanical systems to the quantum ground state or applications such as photonic signal processing.

BIOGRAPHICAL SKETCH

Rob grew up in the small town of Grafton, Massachusetts and attended Grafton Public High School. In 2007 he received his A. B. in Physics from Harvard University, where he did research for Prof. Charles Marcus on novel contrast agents for MRI. He then attended Cornell for his PhD in Applied Physics, where he worked for Prof. Harold Craighead on nanoelectromechanical systems. Rob will continue his scientific work at Columbia University, where he will be an Energy Frontier Research Center Postdoctoral Fellow.

This thesis is dedicated to my family: Bob, Ramona, Christina, Marissa, and Tina.

ACKNOWLEDGEMENTS

I owe a debt of gratitude to the colleagues who gave me my start in the Craighead Group. Thanks especially to Joshua Cross, Leon Bellan, Darren Southworth, Phil Waggoner, Ben Cipriany, Christine Tan, Steve Levy, and Seung-min Park, all of whom have forever shaped me as a scientist. Special thanks go to Rob Ilic, who spent many sleepless nights in the cleanroom with me to make this research possible. Special thanks also to Scott Verbridge, who as my first mentor truly gave me my start in the group and taught me how to use the optical setups inside and out.

I would also like to thank the many group members with whom I have had the pleasure of working for the past several years. These include Kylan Szeto, Daniel Joe, Aline Cerf, Thomas Alava, Yoav Linzon, Juraj Topolancik, Jaime Benitez, Christopher Kelly, David Latulippe, Harvey Tian, Chris Wallin, Bob De Alba, and Nikolay Zhelev. Special thanks go to Vivek Adiga, who taught me what a plate nut was and who built much of the equipment used for the studies of optomechanics.

I have also been fortunate to benefit from an extremely productive collaboration between the Craighead / Parpia Groups and the McEuen Group. Soon after I joined the group, Arend van der Zande inspired me to work on graphene, eventually leading to the topic of this thesis. When Arend left, I also had the pleasure of working with Isaac Storch, whose inquisitive nature and hard work made the study of optomechanics possible. Thanks also to Melina Blees, Sam Roberts, Josh Kevek, and Jonathan Alden, whose willingness to help our group and others on many occasions represents the best of the collaborative spirit at Cornell.

The chapter on "Further Improvements in Quality Factor" demands special acknowledgmenets. Special thanks go to Kylan Szeto for his help on the work

with stretching graphene, and to Sunwoo Lee of Columbia University for his help on the graphene / nitride project. For both projects, the guidance of Arend van der Zande was invaluable.

Thanks to many collaborators both in and out of the group, without whom much of the research described here and elsewhere would not be possible. Among these are Shriram Shivaraman, Julia Mundy, Pinshane Huang, Robert Hovden, Carlos Ruiz-Vargas, Peijie Ong, SiPing Wang, Will Whitney, and many, many more. I would also like to thank the many staff members I have received help from over the years, including Meredith Metzler, Kelly Baker, Garry Bordonaro, Ed Camacho, Noah Clay, Jerry Drumheller, Vince Genova, Phil Infante, Karlis Musa, Daron Westly, Aaron Windsor, Sam Wright, Michael Skvarla, John Treichler, Beth Rhoades, John Grazul, and Mick Thomas. I also had the good fortune to work with some very talented undergraduates, including Diana Wu, Reyu Sakakibara, and Nitin Malik. I also received valuable advice from many of the faculty at Cornell, including Prof. Mukund Vengalattore and Prof. Jiwoong Park. I would also like to thank my undergraduate advisor, Prof. Charles Marcus, for inspiring me to get my Ph.D., and the NSF for funding my research.

Finally, thanks to my advisors for sharing wisdom and many stimulating ideas with me over the course of the last five years. Thanks especially to my minor advisor, Prof. Mike Spencer, and my committee members, Prof. Paul McEuen, Prof. Jeevak Parpia, and Prof. Harold Craighead. In particular, I could not have asked for a better advisor than Harold, who gave me many good ideas and the freedom to explore my own. Thank you for giving me the opportunity to be a part of your group.

TABLE OF CONTENTS

LIST OF FIGURES

Chapter 1

Introduction: NEMS and Optomechanics

1.1 Nanoelectromechanical Systems

The ability to manufacture progressively smaller electronics has been one of the most impressive technological achievements of the past several decades. The most striking example is Moore's Law, which according to Moore's 1975 formulation stipulates that the density of circuit components will double every 18 months [16]. Despite its exponential nature, this prediction has remained true until the present day, with the size of transistor features shrinking from 10 microns to less than 30 nm over the last 40 years [17]. As much as anything, Moore's Law is a testament to human ingenuity and economics, but underlying it is an important fundamental truth about integrated circuit technology. Moore himself summed it up this way in 1995 [16]:

"By making things smaller, everything gets better simultaneously. There is little need for tradeoffs. The speed of our products goes up, the power consumption goes down, system reliability, as we put more of the system on a chip, improves by leaps and bounds, but especially the cost of doing things electronically drops as a result of the technology."

Moore was talking about a very specific technology; namely, the integrated circuit transistor. Because making transistors smaller improves their power consumption, speed, and cost, miniaturization has vastly improved their usefulness. Today, researchers have the ability to make other types of devices at very small size scales. It is therefore worth asking the question: is there another technology that benefits from miniaturization? What besides the transistor might be worth making smaller?

This thesis focuses on the idea that mechanical devices are one such technology. At first, mechanical devices might seem like an odd choice, since the bulk of market adoption for microelectromechanical systems (MEMS) is currently driven by motion sensors like accelerometers [18], whose performance typically worsens at small dimensions [19]. However, there is a class of applications for which smaller mechanical devices offer superior performance, such as mass sensing, force sensing, and cooling mechanical systems to the quantum regime. In these cases, it is worthwhile to make the mass of the mechanical devices as small as possible.

This thesis deals primarily with nanoelectromechanical systems (NEMS), mechanical devices that have at least one dimension smaller than 100 nm. These devices are sometimes further classified into resonant and quasistatic NEMS; here, we will focus mostly on resonant NEMS. The small size of NEMS is crucial to their performance. In reducing the size of NEMS, their mass is reduced, which makes them extraordinarily sensitive detectors of mass, force, and displacement. Here, we will discuss how to mass-manufacture mechanical resonators on even the atomically thin scale for various applications. We will begin with a brief introduction to NEMS.

1.1.1 NEMS Basics

Resonant NEMS contain a mechanically moving component that can be modeled as a harmonic oscillator. The equation of motion for a simple harmonic oscillator, with a driving force F and a damping assumed to be proportional to velocity, is given by

$$F = m\ddot{x} + \gamma\dot{x} + kx \tag{1.1}$$

which for a sinusoidal driving force $F(t) = F_0 cos(\omega t)$ is typically rewritten as

$$Acos(\omega t) = \ddot{x} + 2\beta\dot{x} + \omega_0^2 x. \tag{1.2}$$

where $A = F_0/m$, $\beta = \gamma/2m$, and $\omega_0 = \sqrt{k/m}$ is the resonant frequency.

The steady-state solution is a Lorentzian

$$x_p(t) = \frac{A}{\sqrt{(\omega_0^2 - \omega^2)^2 + 4\omega^2\beta^2}} \cos(\omega t - \delta) \tag{1.3}$$

with

$$\delta = \tan^{-1}\left(\frac{2\omega\beta}{\omega_0^2 - \omega^2}\right) \tag{1.4}$$

Without a consistent driving force, the vibration will eventually stop because of energy lost to damping. The degree of damping is typically characterized in terms of a "quality factor" Q of the system. A useful way to express Q is in terms of energy lost per cycle ΔE relative to the total energy stored in the resonator E.

$$Q = 2\pi\frac{E}{\Delta E} \tag{1.5}$$

For lightly damped oscillations, the Q can also be expressed as:

$$Q = \frac{\omega_0}{\Delta\omega} \tag{1.6}$$

where $\Delta\omega$ is the full width half maximum of the power curve in frequency space (that is, the width of the peak where the amplitude x falls to $1/\sqrt{2}$ its maximum value).

Quality factor can be thought of as the purity of the tone with which a resonator vibrates: the higher the quality factor, the narrower the resonance peak in frequency space. The quality factor of a resonant NEMS device plays an important role in its ability to sense mass and force, as described below.

1.1.2 Applications and Relevant Metrics

Most NEMS sensors work by transducing a change in the quantity of interest (e.g. mass, force) into a change in frequency. If we assume that the readout of the resonance has a background of white noise and a power dynamic range DR, we find the smallest frequency shift that can be resolved [20]:

$$\delta\omega_0 = \frac{\omega_0}{Q} 10^{-DR/20} \tag{1.7}$$

The above equation indicates that improvements in sensitivity can be afforded either by enhancing the possible signal-to-noise ratio $10^{-DR/20}$ or by enhancing quality factor, as will be evident in each of the specific applications discussed below.

Mass Sensing

One of the major applications of NEMS has been mass sensing. This sensing mechanism relies on the fact that the frequency of a resonating mechanical device will change when an analyte is attached to it.

To find the minimum possible mass δm that can be sensed, we use $\omega_0 = \sqrt{\frac{k}{m}}$ to find $\delta\omega_0 = -(\omega_0/2m)\delta m$, which in combination with 1.7 gives [20]

$$\delta m = \frac{2m}{Q} 10^{-DR/20} \tag{1.8}$$

In other words, the minimum resolvable mass is directly proportional to the mass of the device. Because of the dramatic range over which m can be scaled, NEMS are the most sensitive means of directly measuring mass. Viral masses on the femtogram scale were measured in 2004 [21], soon followed by attogram masses [22, 23], zeptogram masses [24], atomic-scale masses [25, 26, 27], and most recently yoctogram masses [28]. The atomic- and yoctogram-scale mass sensing experiments

were all done using carbon nanotubes, which offer the advantage of extremely low mass.

Force Sensing

Another application at which NEMS excel is force sensing. The minimum force that can be sensed is (in $\mathrm{N}/\sqrt{\mathrm{Hz}}$):

$$dF^f = (4k_{\mathrm{eff}}k_B T/\omega_0 Q)^{1/2} \tag{1.9}$$

where k_{eff} is the effective spring constant, k_B is the Boltzmann constant, T is temperature, and ω_0 is frequency.

NEMS devices can be quite sensitive to force. For example, the force sensitivity of ultrasensitive cantilevers used to do magnetic resonance imaging is $dF^f \approx 1$ $\mathrm{aN/Hz^{1/2}}$ at 100 mK [29]. At room temperature, force sensitivities are somewhat more modest, both because temperature is higher and quality factor is lower. For example, the estimated room temperature force sensitivity for the cantilevers in [30] is $dF^f \approx 50$ $\mathrm{aN/Hz^{1/2}}$.

Mechanical Systems in the Quantum Regime

Beyond practical applications, micro- and nanomechanical systems may hold the key to understanding basic physics of mechanical motion [31]. Since the beginning of the 20th century, it has been clear that Newton's Laws are not a complete description of motion. General relativity is required to describe the motion of objects with large masses or large speeds. Quantum mechanics is required to describe the motion of objects at the atomic or subatomic scale. However, while controlling the quantum mechanical motion of individual atoms is routine [32], investigating quantum mechanics at the scale of nanomechanical or micromechanical objects is

not. Investigating quantum mechanics using NEMS has been a research goal for over a decade [33, 34, 35], and might be important both for fundamental science and for applications such as quantum information processing. Before they can fulfill this promise, however, NEMS must first be placed firmly in the quantum regime; that is, they must clearly obey the laws of quantum mechanics rather than classical mechanics.

There are two major figures of merit that characterize mechanical devices in the quantum regime. One is the total thermal occupation, defined as $\overline{n} = k_B T/\hbar\omega_0 - 1/2$. When $\overline{n}$ is below 1, the resonator is in its ground state most of the time [31]. The other important figure of merit is the zero-point motion. Even if the resonator is cooled to its quantum ground state, it will still vibrate with amplitude $x_{zp} = \sqrt{\hbar/2m\omega} = \sqrt{\hbar\omega/2K}$. The primary challenges associated with investigating mechanical systems in the quantum regime are: first, cooling the system (reducing $\overline{n}$), and second, detecting that motion. For the former problem, it is useful to have resonators with high frequency ω. For the latter problem, it is useful to have a resonator with extremely small mass m to increase the zero point motion by as much as possible.

The first demonstration of quantum control of a micromachined resonator solved these challenges using a 6 GHz thin plate oscillator [36]. Because the frequency was so high, the quantum regime $k_B T < \hbar\omega$ could be reached using conventional cryogenic cooling in a dilution refrigerator to $T \approx 25$ mK. Read-out and control of mechanical motion were accomplished by strongly coupling the piezoelectric mechanical resonator to a resonant superconducting quantum circuit. This experiment demonstrated for the first time that a man-made mechanical oscillator could be cooled to its quantum ground state. However, the relatively low mechanical quality factors ($Q \approx 260$) and correspondingly short mechanical state

lifetimes prevented direct tests of quantum entanglement and complicated operations on the mechanical states. In addition, the extremely small zero point motion ($x_{zp} \sim 10^{-16}$ nm) prevented investigations of quantum superpositions [37]. Ideally, the quantum ground state could be reached for lower-frequency oscillators that have higher quality factors, but for lower ω, an advanced refrigeration technology is necessary to reach $\overline{n} < 1$. In the next section, we will describe how tools from the field of optomechanics can provide the requisite cooling.

1.2 Optomechanics

Optomechanics [1, 38] is the science of using the forces associated with light in order to manipulate mechanical objects. Low-mass mechanical resonators provide enormous advantages for optomechanical applications, since low mass translates into low stiffness $K = m\omega^2$, which in turn makes the structures more sensitive to the (relatively weak) forces of light. Therefore, although optomechanical effects are important on a wide variety of size scales, including for km-scale gravitational wave detectors and gram-scale mirrors [39], optomechanics research has seen renewed interest as a result of developments in MEMS and NEMS.

Typically, optomechanics involves the use of so-called "back-action" forces to manipulate the damping in a resonator. Back-action is broadly defined as occurring when a measurement influences the motion of a probed object; in its simplest form, feedback from a probe can influence the damping of a resonator [31]. Many applications for these types of effects have emerged, including force sensing [40], non-volatile mechanical memory [41], and photonic signal processing [42, 43]. However, research in optomechanics has primarily focused on using feedback and other back-action forces to cool MEMS and NEMS resonators toward the quantum ground state as described above. We will first trace the development

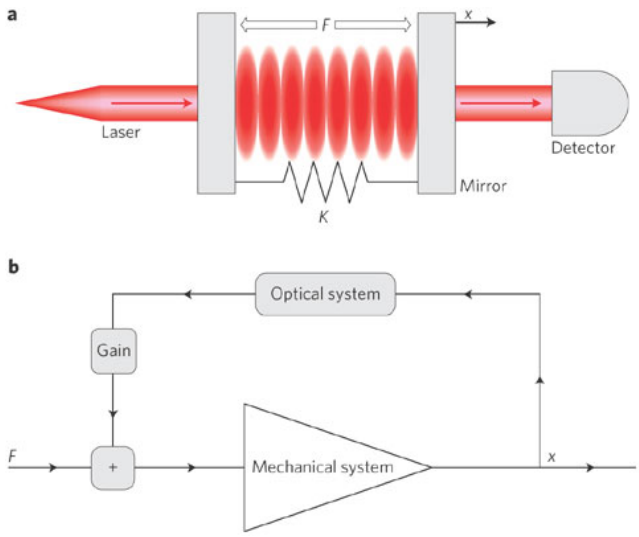

Figure 1.1: (a) A canonical optomechanical system. Two mirrors trap light, forming a Fabry Perot cavity with the light exerting a back-action force F on the mirrors. When one mirrors moves, the amount of light stored in the cavity changes, thereby changing the force on the mirrors. This feedback effect can be modeled as illustrated in (b) and forms the basis for optomechanical modification of damping. Reproduced from [1].

of modern optomechanics by reviewing these cooling results, then introduce the other remarkable achievements of optomechanics.

1.2.1 Cooling

In early work, light was used to manipulate the damping in a MEMS device in 2001 by placing the resonator in a laser standing wave [44]. Later, a cavity between a metal-coated fiber-optic cable and a metal-coated cantilever [45] was used to cool a resonator from room temperature to 18K by exploiting photothermal forces [46]. The basic premise in these experiments was that a delayed feedback effect resulting from laser heating resulted in a force proportional to the oscillator's velocity, thus modifying the damping (Figure 1.1). If that force opposes the resonator's motion,

then the motion of the resonator can be confined, effectively "cooling" it. Soon afterward, optomechanical cooling utilizing radiation pressure forces was demonstrated in several laboratories [47, 48, 49, 50], setting off a race to cool a MEMS or NEMS resonator to its quantum ground state.

As mentioned above, ground state cooling was first achieved by conventional refrigeration techniques [36]. Soon afterward, other teams achieved optomechanical cooling to the quantum ground state [51, 52]. In the case of optical cooling [52], the ground state was reached by applying a laser to a resonator at 20K - a base temperature 3 orders of magnitude larger than that in [36]. This effectively eliminated the need for a dilution refrigerator while operating at $\omega_0 = 3.68$ GHz and $Q = 10^5$.

1.2.2 Radiation pressue vs photothermal forces

Except for the first MEMS cooling result [46], all of the abovementioned developments in cooling a mechanical resonator to its quantum ground state utilized radiation pressure rather than photothermal forces. Radiation pressure has become the preferred approach for cooling resonators for several important reasons. First, photothermal forces arise from heat and are therefore inherently dissipative. This precludes quantum-coherent transfer of information between optical photons and phonons in the resonator [53]. Second, photothermal forces are more difficult to describe in quantum mechanical formalism than radiation pressure forces and therefore present theoretical challenges.

However, photothermal forces do play a very important role in optomechanics. It has been shown theoretically that photothermal forces are capable of cooling a resonator to its quantum ground state [54, 55]. Furthermore, photothermal forces can be orders of magnitude stronger than radiation pressure forces and in some

cases may be superior for cooling to the quantum ground state [56]. Thus, it is well established that photothermal forces are useful for cooling. To establish quantum-coherent coupling to a photothermally cooled resonator, one could, for example, couple the resonator to a single electron via charge [57] or spin [58].

1.2.3 Self-oscillation

The opposite of optomechanical cooling is feedback that effectively *decreases* the damping in a resonator. This can result in optomechanical self-oscillation, in which a resonator's damping is reduced to near zero by optomechanical back-action and the thermal fluctuations are enough to set it into motion. Like cooling, optomechanical self-oscillation was first demonstrated using photothermal forces in silicon discs [44] and cantilevers [46]. In 2005, the same effect was observed for radiation pressure [59]. Optomechanical self-oscillation could be particularly useful for photonic signal processing applications, such as photonic-RF downconversion [42]. In addition, a self-oscillating resonator displays nonlinear behavior such as frequency entrainment, in which the vibrations synchronize with a small "pilot" drive signal [60, 61]. This phenomenon could be use to amplify the pilot signal or filter out unwanted frequencies. Injection locking could also be used to synchronize two optomechanical oscillators using an optical carrier signal, which could potentially be useful for communication over long distances.

The nonlinear dynamics of self-oscillating systems are also interesting. In a system comprising a Fabry-Perot cavity with one end mirror attached to a vibrating cantilever, a complex phase diagram involving multistability regions (multiple solutions for amplitude at a given deflection) was recently observed [62]. In addition, chaotic behavior has been observed in optomechanical toroidal and spherical resonators [63].

It is worth mentioning that self-excited vibrations can be realized by other means. For example, optomechanical self-oscillation is analagous to self-oscillation induced by direct electrical feedback [64].

1.2.4 Important Metrics

Displacement Sensitivity

One of the most impressive achievements of optomechanics is extremely precise displacement sensitivity. Typically, optical interferometry is used to measure mechanical displacement, with sensitivities reaching 10^{-18} m $\mathrm{Hz}^{-1/2}$ [65, 66]. For measuring NEMS, this sensitivity is superior even to that of single electron transistors, which have achieved sensitivities of 2×10^{-15} m $\mathrm{Hz}^{-1/2}$ [67]. Achieving high displacement sensitivity is essential for measurement of mechanical systems in the quantum regime, as discussed in Section 1.1.2.

Optomechanical Coupling

A good optomechanical system has a strong degree of coupling between the mechanical and optical elements. For radiation-pressure coupling between an optical cavity with optical resonance frequency Ω and a mechanical resonator acting as one of the mirrors of the cavity (see Figure 1.1), the interaction energy between optical and mechanical degrees of freedom governed by the "vacuum optomechanical coupling rate" [68, 69]:

$$g_0 \equiv G \times x_{zp} \tag{1.10}$$

where $G = \frac{d\Omega}{dx}$ is the optomechanical coupling coefficient and x_{zp} are the zero-point fluctuations discussed in section 1.1.2. The vacuum optomechanical coupling rate gives the per-photon coupling rate between the systems; coupling can be enhanced

by increasing the number of photons in the cavity, $\sqrt{\overline{n_c}}$. The quantum coherent coupling regime is reached when the rate at which the optical and mechanical systems exchange energy, $\Omega_c = 2\sqrt{\overline{n_c}}g_0$, is greater than either the optical decoherence time κ or the mechanical decoherence rate $\gamma = k_B T/\hbar Q$.

We can gain some insight into the ideal optomechanical system by recalling the formula for zero-point motion: $x_{zp} = \sqrt{\hbar/(2m_{\text{eff}}\omega)}$. Again, we see that resonators with low mass provide a crucial advantage to quantum optomechanical systems by boosting vacuum optomechanical coupling rate. This thesis will discuss manufacturing optomechanical NEMS from the thinnest possible material, graphene, and explore the impact of the advantages provided by its ultralow mass.

Chapter 2

Graphene Nanoelectromechanical Systems

2.1 Introduction to Graphene

Graphene, a single layer of carbon atoms in a honeycomb lattice, is a material of both scientific interest and technological promise [70, 2]. It has remarkable electronic properties, including the fact that its electrons have zero effective mass, so that it offers a window into the physics of the Dirac equation [71]. The combination of its two-dimensional geometry and its electronic properties, including ultrahigh electron mobility [72], make it useful for a number of technologies, including chemical sensors [73], flexible and transparent electrodes [74], and high-frequency analog transistors [75, 76]. In addition to its electrical properties, graphene has unique mechanical properties. It is the strongest material ever measured, with a breaking strain of nearly 25%, and it is among the stiffest known materials, with a Young's modulus of 1 TPa. Therefore, it has also been suggested for use in mechanical applications such as switches [77], membranes separating disparate environments, [78, 79, 80, 81] and supports for transmission electron microscopy [82].

Among the devices for which graphene appears almost ideally suited are nanoelectromechanical systems. As we have discussed, the small size of NEMS is crucial to their performance. In reducing the size of NEMS, their mass is reduced, which has benefits for mass and force sensing and for mechanical systems in the quantum regime. The ultimate limit would be a resonator one atom thick, but reducing most materials to such small dimensions generally affects mechanical stability and stiffness. Graphene, however, is simultaneously one atom thick

and enormously strong and stiff. Additionally, its electrical conductivity enables integrated electrical transduction, and its planar geometry lends itself easily to standard lithographic processing. Graphene's suitability for mechanical resonance applications has already been demonstrated in many experiments.

This thesis discusses methods producing large arrays of high-quality graphene NEMS and their applications. This chapter will provide an introduction to the field of graphene nanomechanics and review the challenges associated with building a new class of two-dimensional resonator from graphene. We will begin with the production of graphene and then discuss work by this author and others on reproducibly manufacturing large arrays of graphene resonators. Much of this chapter is reproduced from [83].

2.2 Graphene Production

Since graphite is composed of many stacked layers of graphene, simply rubbing graphite against a solid surface produces graphene. However, many attempts to fabricate graphene by this method produced only multilayer graphene that was difficult to locate [84, 85, 86, 87, 88]. The recent explosion of graphene research was enabled by the discovery that monolayer graphene is visible in an optical microscope if it has been isolated on a layer of oxide of precisely chosen thickness on a silicon wafer [70, 89, 90, 91]. The visibility of graphene under these conditions, which is due to optical interference, enabled rapid examination of large surface areas to determine where single layer graphene is produced by even a very low throughput method. Thus, rubbing thin flakes of graphite on top of SiO_2 on silicon, which yields few samples of single layer graphene in a wide assortment of multilayer stacks, became a viable method of producing graphene. This technique, called "mechanical exfoliation," is shown in Figure 2.1a; the visibility of graphene

on an appropriate thickness of SiO_2 is shown in Figure 2.1b. While optical interference allows single layers of graphite to be distinguished from multiple layers, it was soon discovered that the number of layers in a stack of graphene sheets could be determined from its Raman spectrum, which enabled more quantitative confirmation that a given sample was indeed monolayer graphene [92, 93]. Being able to optically identify potential single layer candidates and confirming their thickness with Raman spectroscopy enabled production of the first suspended graphene sheets via mechanical exfoliation, as we will discuss.

Mechanical exfoliation of graphene is still common practice today. However, locating graphene amid the assortment of thicker graphite produced by mechanical exfoliation is painstaking work, and the technique is not scalable. Fortunately, a number of other techniques are used to fabricate graphene in large areas. Epitaxial graphene growth, in which graphene is formed by sublimating silicon from silicon carbide, has been used to grow large-area, several-layer-thick graphene sheets that behave like graphene [94, 95], Two-dimensional assemblies of reduced graphene oxides have also been heavily studied [96, 97, 98] and although they do not exhibit the electronic properties of graphene, they exhibit excellent mechanical properties [99] and may be well suited for NEMS.

Another approach is to grow graphene on metals by chemical vapor deposition (CVD). In early steps toward this method, graphene was synthesized on ruthenium [100] and iridium [101]. For device fabrication purposes, a major achievement was the growth of few-layer graphene on nickel, which allowed both large-area growth and isolation of the graphene from the metal [102, 103]. Unfortunately, graphene growth on nickel was characterized by regions with large numbers of layers. Soon thereafter, graphene growth by chemical vapor deposition on copper was found to produce up to 95% single layer graphene, with most of the rest bilayer

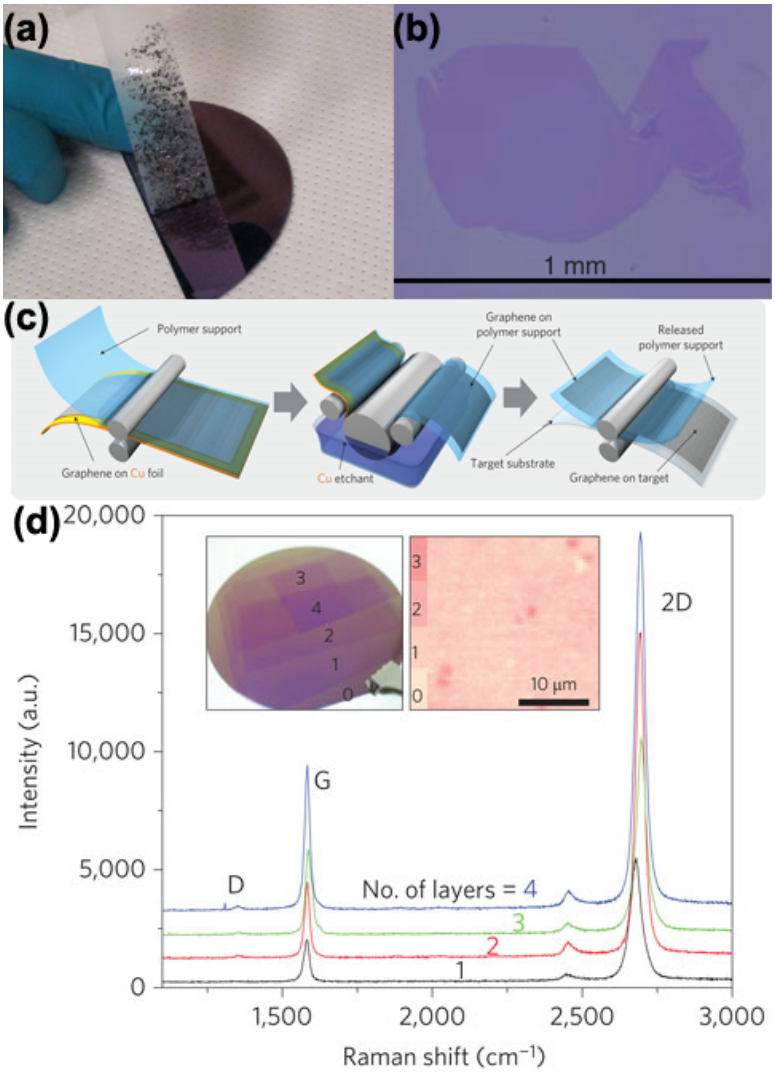

Figure 2.1: (a) Synthesis of graphene by mechanical exfoliation. Graphite is thinned by repeatedly peeling layers apart with scotch tape, then rubbed against a layer of oxide on a silicon wafer. (b) An exceptionally large graphene flake obtained by exfoliation. Reproduced from Ref [2]. (c) Schematic for producing large-area graphene from graphene grown on copper foil, adopted from Ref [3]. Graphene is produced on a roll of copper foil and attached to a polymer support using light pressure between two rollers. Using additional rollers, the copper is dissolved and the graphene is transferred to the final substrate. (d) The results of a similar process on a silicon wafer, together with an optical image showing more than 95% monolayer coverage. Reproduced from Ref. [3].

graphene [104]. Since this discovery, much progress has been made in growing graphene by CVD on copper [3], including production of graphene on rolls of copper (Figure 2.1 c-d) and the production of graphene from solid sources on copper using temperatures as low as 800 ° C. Recent studies of graphene produced by CVD on copper showed that it is polycrystalline [105, 106] and that its mechanical strength was weakened at its grain boundaries [107]. However, slightly modified growth methods have been observed to produce graphene with much larger grain sizes [108]. It is suspected that further work on this growth method will yield graphene with fewer bilayer regions and larger grain sizes.

2.3 The First Graphene Resonators

2.3.1 Fabrication

The first suspended graphene sheets were produced using mechanical exfoliation, relying on the ability to identify graphene on an oxide surface [92, 4, 109]. In one method [92, 109], graphene sheets were produced by mechanical exfoliation on a standard SiO_2 surface and modified by e-beam lithography and etching to produce suspended graphene sheets on a metallic scaffold for transmission electron microscopy. In another experiment [4], mechanical exfoliation was used to fabricate graphene on top of predefined trenches in SiO_2, resulting in a doubly clamped beam that was confirmed to be monolayer graphene by Raman spectroscopy (Figure 2.2a-b). In both cases, only a small number of samples were produced. Nonetheless, the advent of suspended graphene proved very useful for the graphene community. Bolotin et al. showed that suspended graphene could be used to achieve ultrahigh electron mobility [72], making exfoliated suspended graphene instrumental in the recent observation of the fractional quantum hall effect in graphene [110, 111]. It

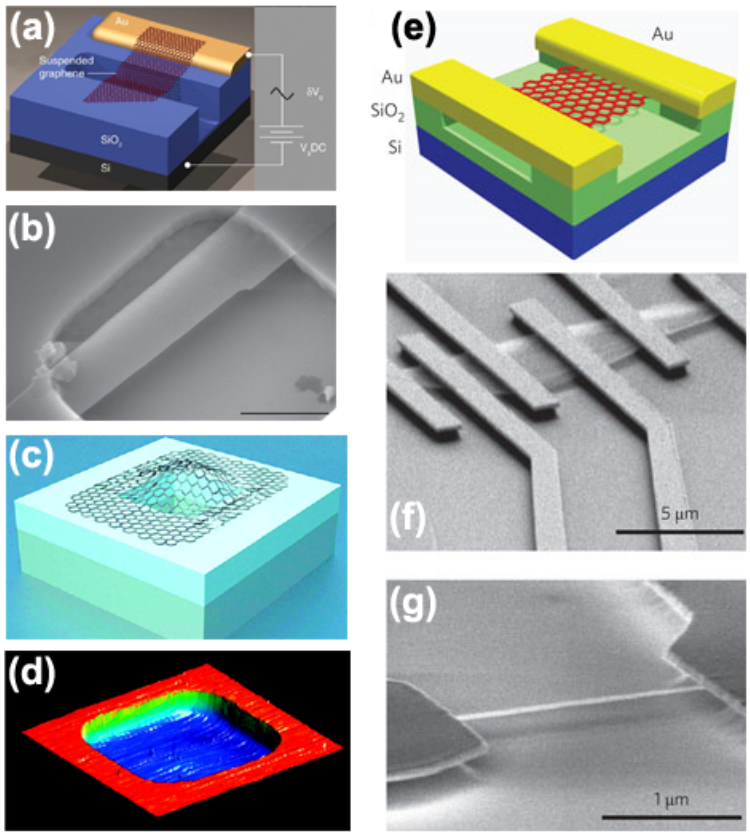

Figure 2.2: Graphene resonators made using exfoliation. (a-b) Schematic and SEM image of a graphene resonator made by mechanically exfoliating graphene over a trench, reproduced from Ref. [4]. (c-d) Schematic and AFM image of a graphene resonator made by exfoliating graphene over a well. The graphene sheet (c) bulges upward in response to pressure, and (d) self-tensions by adhering to the sidewalls of the well when not acted on by other forces. Reproduced from Ref. [5]. (e-g) Schematic and SEM images of graphene resonators fabricated by mechanical exfoliation followed by lithographic processing. Reproduced from Ref. [6].

is also possible to produce enclosed volumes sealed by exfoliated graphene [5], as in Figure 2.2(c-d), and to use lithography to produce arrays of graphene resonators of different lengths and shapes from exfoliated graphene, as shown in Figure 2.2(e-g) [6]. Mechanical exfoliation is still used today to produce mechanical resonators [112] and other types of devices from graphene because it yields strips of very clean graphene without the need for lithography. Additionally, the continual refinement of the exfoliation technique has enabled the production of very large suspended graphene sheets with dimensions on the order of 50 microns [113]. However, the technique is not scalable to producing large numbers of devices.

2.3.2 Detection of Graphene Resonance

Optical Detection

In addition to fabricating devices, we have developed means of measuring their motion. To optically monitor mechanical resonance, a continuous wave (CW) laser impinges on the cavity and reflected laser light is modulated by an amount proportional to $\Delta z(\omega) dR/dz$, where $\Delta z(\omega)$ is the amplitude of the vibration at a given frequency ω. The reflected light is monitored by a fast photodiode connected to a network analyzer. We will now derive the expected amount of modulation in the reflected light.

Consider a Fabry-Perot cavity formed by a graphene sheet suspended some distance d above a perfectly reflective backplane. We calculate the overall cavity reflectivity in terms of the electric field of the incident and reflected plane waves, $R = |E_{reflected}|^2/|E_{incident}|^2$, as a function of position of the graphene membrane. We start by assuming the graphene is an infinitely thin conducting sheet with a reflection coefficient r_g, a transmission coefficient t_g, and a distance d away from a perfectly conducting back plane (see e.g. the model in Figure 2.2a). Summing

over contributions from every reflected wave, the reflection coefficient of the cavity is given by

$$r = -\left(r_g + \frac{t_g^2 e^{i\phi}}{1 - r_g e^{i\phi}}\right)$$

where $\phi = 4\pi d/\lambda$ is the phase difference obtained from one round trip inside the cavity. The minus sign accounts for the phase shift due to reflection off a conducting surface; each wave contributing to the sum reflects an odd number of times. The cavity reflectivity is then given by the magnitude of the reflection coefficient squared:

$$R = |r|^2 = r_g^2 - t_g^2 + \frac{t_g^2(1 - r_g^2 + t_g^2)}{1 + r_g^2 - 2r_g \cos\phi} \tag{2.1}$$

The transmittance and reflectance of graphene can be found by applying Maxwell's equations and the appropriate boundary conditions at the graphene, while assuming the conductivity is small [113, 114]: $T_g = (1 + \pi\alpha/2)^{-2}$, $R_g = (\pi\alpha)^2 T/4$, where $\alpha = 1/137$ is the fine structure constant. The reflection and transmission coefficients are then found by taking the square root:

$$r_g = \frac{\pi\alpha}{2 + \pi\alpha}$$

$$t_g = \frac{2}{2 + \pi\alpha}$$

Plugging these into Eq. 2.1 gives the cavity reflectivity as a function of cavity detuning, which we have plotted in Figure 2.3.

Figure 2.3 is one of the most useful results in this document. It says that the light reflecting from graphene suspended above a mirror varies by more than 8% depending on the location of the graphene. This strong variation enables us to read out the motion of a graphene resonator with high sensitivity.

Electrical Detection

There are also several means of electrically detecting graphene motion. These will be discussed in Section 2.4.

2.3.3 Actuation of Graphene Resonance

Actuating motion of most graphene NEMS has proven simpler than detecting it. Both electrical and optical drive methods have been used to drive graphene over its full dynamic range; that is, from a minimum vibrational amplitude comparable to thermal fluctuations to a maximum vibrational amplitude characterized by the onset of Duffing nonlinearity [115]. In most cases, electrical drive uses capacitive attraction to drive the motion of the resonator relative to a gate [4, 6, 116]. The optical method utilizes a strobed laser whose light is partially absorbed by the graphene sheet, so that the sheet is periodically heated and cooled at the driving frequency; thermal expansion and contraction then convert these temperature changes into device motion [4, 15]. Using the optical method, resonator motion can be monitored without fabricating electrodes, which allows resonators to be examined with minimal resist contamination.

It is worth noting that other drive mechanisms hold much promise for graphene NEMS. In particular, nonresonant oscillatory motion of very small, high-frequency resonators has been actuated and detected using scanning tunneling microscopy [117]. These devices have an estimated frequency of 400 GHz and could allow highly sensitive mass detection or exploration of quantum behavior in mechanical oscillators. However, driving the resonant motion of these devices will be challenging.

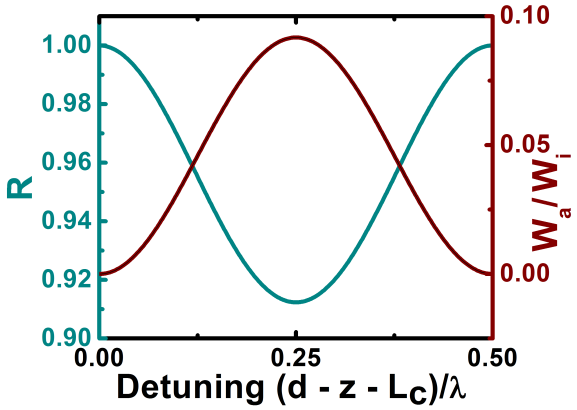

Figure 2.3: Calculated cavity reflectivity R and graphene absorbed energy flux W_a normalized by the incident energy flux W_i as a function of detuning from the resonant cavity length L_c.

2.3.4 Results and Limitations

The first graphene resonator was actuated and detected using optical methods, yielding a fundamental frequency $\omega_0 = 2\pi \times 70.5$ MHz with Q = 78 [4]. Temperature dependence and gate voltage dependence were also investigated, which were consistent with later studies that we will discuss in more detail.

This experiment demonstrated that graphene could be used as a mechanical resonator, but also revealed important roadblocks to adoption of graphene for NEMS. First, the quality factor was very low, precluding applications such as ultrasensitive mass sensing. Second, because the devices were made by mechanical exfoliation, they were difficult to fabricate. Third, scanned probe studies of mode shapes demonstrate that the mode shapes of graphene sheets exfoliated over a trench are unpredictable due to the difficulty of controlling strain and geometry [118]. Finally, the lack of electrodes on both sides of the resonator prevented current-based electrical readout. Current-based readout was eventually achieved simply by fabricating electrodes on both sides of the graphene and using a technique

that we will discuss in the next section. Solving the other problems was a focus of this dissertation, and we will discuss our solutions in section 2.5 and Chapter 3.

2.4 Electrical Control of Graphene Resonators

2.4.1 Electrical Readout

Electrical transduction was demonstrated in graphene [6] using a technique first developed to detect the motion of carbon nanotubes [119]. This technique overcomes the high-frequency impedance issues associated with monitoring electrical signals from nanomechanical resonators by using the resonator itself to mix down the signal to a lower frequency. The measurement is accomplished by suspending a graphene sheet above a backgate between two electrodes (source and drain). A d.c. voltage is applied to the gate in order to tension the device, while an oscillating gate voltage at frequency f is applied to the gate to drive resonator motion via capacitive attraction. A second r.f. voltage at frequency $f + \Delta f$ is applied to the source. Because the graphene conductance G changes with distance from the gate, G oscillates with frequency f on resonance, while the source-drain voltage V is oscillating with frequency $f + \Delta f$. The result is a mixed-down source-drain current $I = VG$ at Δf. For graphene, this technique gives ~ 60 dB dynamic range while allowing frequency tuning of $\sim 100\%$ via the backgate [6]. Variations on this method have been demonstrated to improve signal to noise even further [120].

The major drawback of the mixing technique is its speed [112]. Operating at the frequency Δf (typically $\sim$ 1 kHz) significantly limits operation bandwidth and prevents r.f. applications of these oscillators that would require direct readout of frequency. To transduce the motion of NEMS at MHz frequencies, however, one needs to increase the RC-limited cutoff frequency. In systems with a global

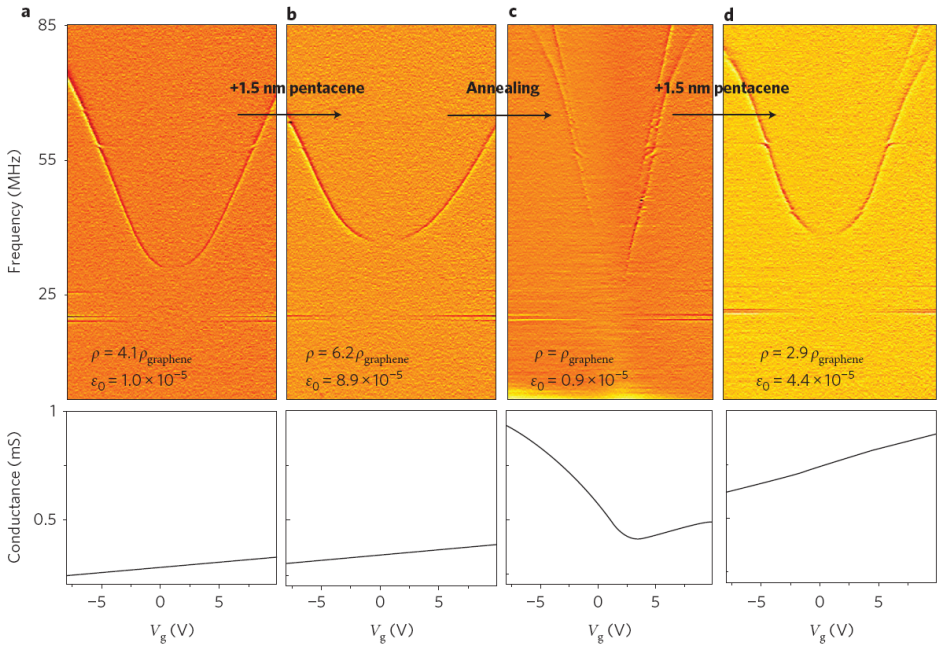

Figure 2.4: Electrically contacted graphene resonators can sense mass, tension, and charge simultaneously. In a color plot of dI/df as a function of frequency f and gate voltage, the graphene resonance stands out as a U-shaped feature. The dependence of the resonant frequency on gate voltage can be fit to extract the density ρ and strain ϵ_0 of the graphene sheet. Here, the deposition of pentacene on an as-fabricated exfoliated graphene resonator (a) causes the measured density and tension to increase (b). (c) Subsequent cleaning restores the density of the sheet to that of a pristine graphene resonator. (d) The addition of more pentacene increases the mass and the stress in the graphene. For each step, the charge can be studied by looking at the plots of conductance versus gate voltage. Figure adopted from [6].

.

backgate (often, the entire wafer acts as the gate), this cutoff frequency is set by unnecessary stray capacitance between the source and drain electrodes and the gate. Xu et al. eliminated this problem by employing a local backgate to reduce stray capacitance [112]. In this geometry, current across a source and drain was measured while a driving force was applied to the resonator by the local backgate. They found that the resonance could be observed through the change in current at the resonant frequency of the device due to the gate-tunable conductance of the graphene. At the expense of more stringent fabrication, this technique allowed them to acquire a given data set 100 times faster than with the mixing technique, while maintaining comparable signal to noise.

2.4.2 Frequency Tuning

Because of graphenes remarkable thinness and flexibility, its frequency can be adjusted over a wide range by applying electrostatic tension via a backgate. See Figure 2.4 for the resonant frequency of one graphene resonator as a function of gate voltage. The strong dependence of frequency on gate voltage is promising for signal processing applications requiring a tunable frequency source. For example, graphene resonators could be useful as tunable filters for wireless communication applications.

Because graphene is both electrically and mechanically active, it can be used to simultaneously sense mass, stress, and charge. The data from one such experiment on an exfoliated graphene resonator is presented in Figure 2.4. Before and after deposition of the analyte pentacene, the resonant frequency is plotted as a function of gate voltage V_g, which allows determination of the mass and stress by fitting the curve to the function:

$$f(V_g) = \frac{1}{2L}\sqrt{\frac{T_0 + T_e(V_g)}{\rho w}} \tag{2.2}$$

where L, w, and ρ are the length, width, and density of the resonator, T_0 is the inherent tension in the device, and T_e is the tension induced by the gate voltage. Simultaneously, the conductance as a function of gate voltage is measured. When 1.5 nm pentacene is evaporated on an exfoliated graphene transistor, the mass of the device goes up, the stress increases, and the charge neutrality point moves to the right. After cleaning via ohmic heating, the charge neutrality point moves to near zero gate voltage, and the resonance becomes more tunable, consistent with the pentacene leaving the device. These measurements demonstrate that graphene can simultaneously sense mass, force, and charge, which has numerous applications; for example, the simultaneous sensing of mass and charge of an analyte would be analogous to mass spectrometry. In addition, a similar way of reading out stress was also used for more fundamental studies of the thermal expansion of graphene [116].

2.5 Large-Scale Arrays of Graphene Resonators

With detection and electrical control of graphene resonators established, one of the most important remaining problems is fabrication. All of the graphene resonators we have discussed were fabricated using mechanical exfoliation, a random process by which it is very difficult to make many devices. Here, we will discuss how to fabricate large arrays of graphene resonators by starting with large-area graphene. Much of this chapter is reproduced from [9].

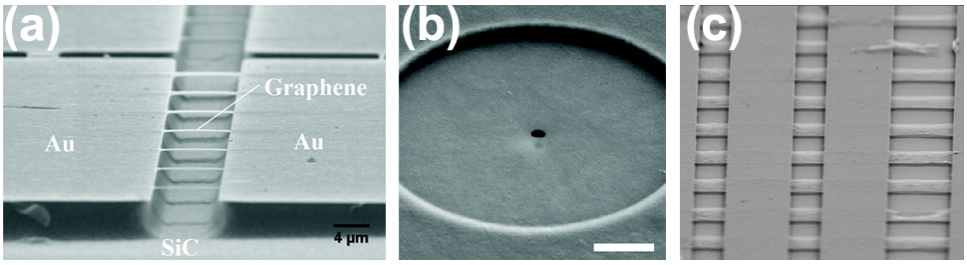

Figure 2.5: Graphene resonators made using large-area graphene. (a) Epitaxial graphene resonators fabricated by shaping the graphene on SiC and undercutting it using a wet etch [7]. (b) Resonators made of reduced graphene oxide. Scale bar, 1μm [8]. (c) Arrays of doubly clamped beam resonators (2 and 5 μm in length) made from CVD graphene [9].

2.5.1 Fabrication

A scalable means of graphene device production involves first growing a large area sheet of graphene and subsequently processing it to create devices. In some cases, the graphene can be processed on the surface on which it was grown. For example, it is possible to grow graphene on top of copper and subsequently remove the copper, resulting in arrays of field effect transistors [121]. Similarly, it is possible to fabricate suspended graphene for TEM studies by selectively etching copper from beneath graphene grown by CVD [122]. It is also possible to make nanomechanical resonators by, for example, etching silicon carbide from beneath graphene grown epitaxially on SiC (Figure 2.5a) [7]. However, the substrates on which graphene can be grown are not necessarily the ideal substrates for devices. For example, the nanomechanical devices fabricated in Ref. [7] were electrically shorted to their doped SiC substrate and could not be probed electronically. For this reason, we focus on what has been the primary approach to creating graphene mechanical devices thus far, which is growing graphene and subsequently transferring it to another surface for processing.

Transferring graphene after its growth is often necessary for a number of reasons. First, CVD growth from gaseous sources requires temperatures greater than 900°C, which poses a challenge for semiconductor processing [123]. Second, the small-scale patterning required to make graphene devices is more easily done on standard silicon wafers than on the metal that facilitates graphene growth. Finally, it is often useful to isolate the graphene from the substrate on which it is usually grown, as in the case of the SiC-derived devices mentioned above. Currently, the most widely employed transfer method begins with graphene grown on copper, which we will discuss in detail here. However, transferring graphene produced by other methods, including mechanical exfoliation [124] and CVD graphene on nickel [77], has been useful for many applications. It is also possible to make few-layer graphene resonators out of reduced graphene oxide transferred to a patterned substrate (see Figure 2.5b) [8].

The transfer of graphene from copper follows earlier procedures developed to transfer graphene from nickel [103]. Following growth of graphene on copper, the graphene is typically coated with a thin polymer layer such as PMMA [104] or thermal release tape [3] to maintain mechanical stability during transfer. Then, the copper is removed by etching with a chemical such as ferric chloride or ammonium persulfate. We note that ferric chloride has been observed to contaminate the surface of graphene with iron [105, 122], which is problematic for some applications. Following the dissolution of copper, the graphene is rinsed in water and brought into contact with the final substrate. Finally, the support layer is removed to leave single layer graphene on an arbitrary surface. Typically, PMMA has been removed using acetone [125], methylene chloride [9], or thermal decomposition at 300°C [126].

This transfer method is robust and can be used to make mechanical devices of

many shapes and sizes. For example, to make the electrically contacted, doubly clamped beam resonators shown in Figure 2.7(a), CVD-grown graphene was transferred to SiO_2, patterned using lithography and oxygen plasma, and contacted by evaporated electrodes. Then, a buffered oxide etch was used to remove the oxide from beneath the device, leaving it free to resonate. In another approach to making doubly clamped graphene beam resonators, graphene was patterned into strips while it was still on the copper using lithography and oxygen plasma. Then, the typical transfer process was used to place the strips on top of prefabricated trenches or electrodes (Figure 2.5c). A similar approach was used to make mechanical switches out of graphene [77]. Fabricating mechanical devices from graphene does not require shaping graphene lithographically. In the Chapter 3, we will describe a way of fabricating drumhead resonators by transferring graphene onto a circle in silicon nitride.

2.5.2 Results

In Ref. [9], we measured many devices of the kind shown in Figure 2.5c; results are shown in Figure 2.6. Figure 2.6a is a plot of the fundamental mode for a doubly clamped membrane of length $L = 2\mu$m and width $W = 3\mu$m. The resonance frequency is $f_0 = 9.77$ MHz and the quality factor is $Q = 52$. Figure 2.6(b-d) shows the frequency and quality factor of the fundamental mode for 38 identically patterned membranes measured along a single trench. Figure 2.6(b-c) are histograms of the resonance frequencies and quality factors. There is a peak in the histogram at $f_0 = 15$ MHz with a spread of 8 MHz. The quality factors range from 25-250 with a peak at 70. Figure 2.6d shows that higher frequency is correlated with higher quality factor. These resonators are nominally identical so the variation is due to either differences in adsorbed mass or the strain and

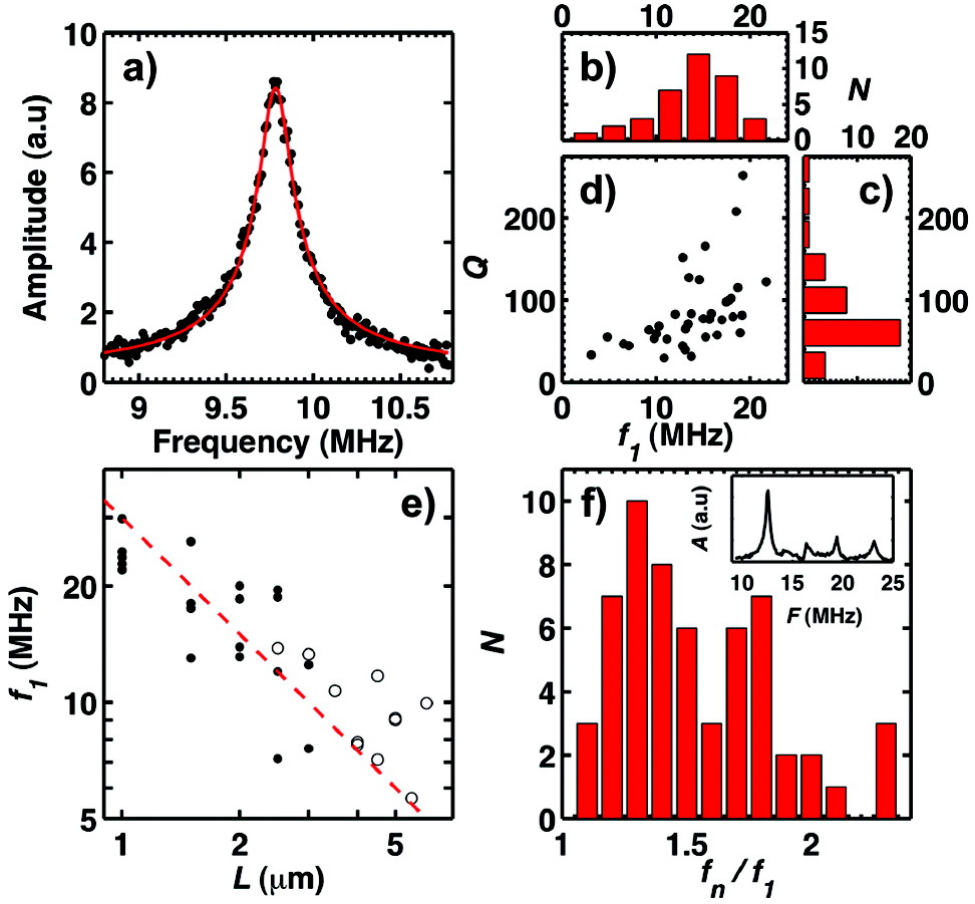

Figure 2.6: (a) Optical interferometry measurement of a fundamental mode for doubly clamped graphene resonator like those shown in Figure 2.5c. $L = 2\mu$m, $W = 3\mu$m. Histogram of the frequency (b), and quality factor (c) of fundamental modes for 38 identical resonators along a single trench $L = 2\mu$m, $W = 3\mu$m. (d) Quality factor versus resonance frequency for the same devices as panels b,c. (e) Fundamental mode frequency versus length for membranes with widths W between 2.5 and 5 μm. Solid dots are continuous, damage-free membranes, open circles are membranes with partial tears in them. Dashed line shows data scales as $1/L$. (f) Histogram of all measured higher modes divided by the fundamental mode for same devices as (b-d). Typical resonance spectrum inset.

.

conformational structure of the membranes.

Figure 2.6e shows f_0 versus L for these doubly clamped membranes with L between 1 and 6μm and W between 2.5 and 5 μm, plotted on a log-log scale. The resonance frequencies decrease with length and show no discernible dependence on the width. For reference, the dashed line shows an L^{-1} dependence. The black dots represent graphene membranes without tears, while the squares represent partially torn membranes. Interestingly, the torn membranes show similar behavior to the untorn membranes.

The tensioned membrane model predicts a second harmonic at twice the frequency of the first. Figure 2.6f shows all measured higher resonant modes of the identical devices, normalized by the fundamental mode frequency with one example spectrum in the inset. Instead of a peak at $2f_0$, there is a broad distribution in frequencies with peaks around $f_n \sim 1.3f_0$ and 1.6 f_0. These peaks correspond with the second and third measured modes. These most likely correspond to transverse modes or edge modes in the resonator due to nonuniform strain in the resonator. Previous experiments [118] have shown that local modes exist in exfoliated graphene resonators and the frequencies of these modes are difficult to estimate without a detailed knowledge of the structure in the transverse direction.

We tested the hypothesis that transverse properties are important in [9] and found preliminary evidence that clamping the membranes on all sides improved the membrane spectra. We will expand upon these claims in the next section.

Some of the most exciting properties of exfoliated graphene resonators are their ability to be actuated and detected electrically [6], their large voltage-tunable frequency range and their high quality factor at low temperature ($Q \sim 10,000$ for exfoliated graphene at 4 K). We explored these aspects of CVD graphene resonators by fabricating electrically contacted devices like those shown in Figure 2.7a. Trans-

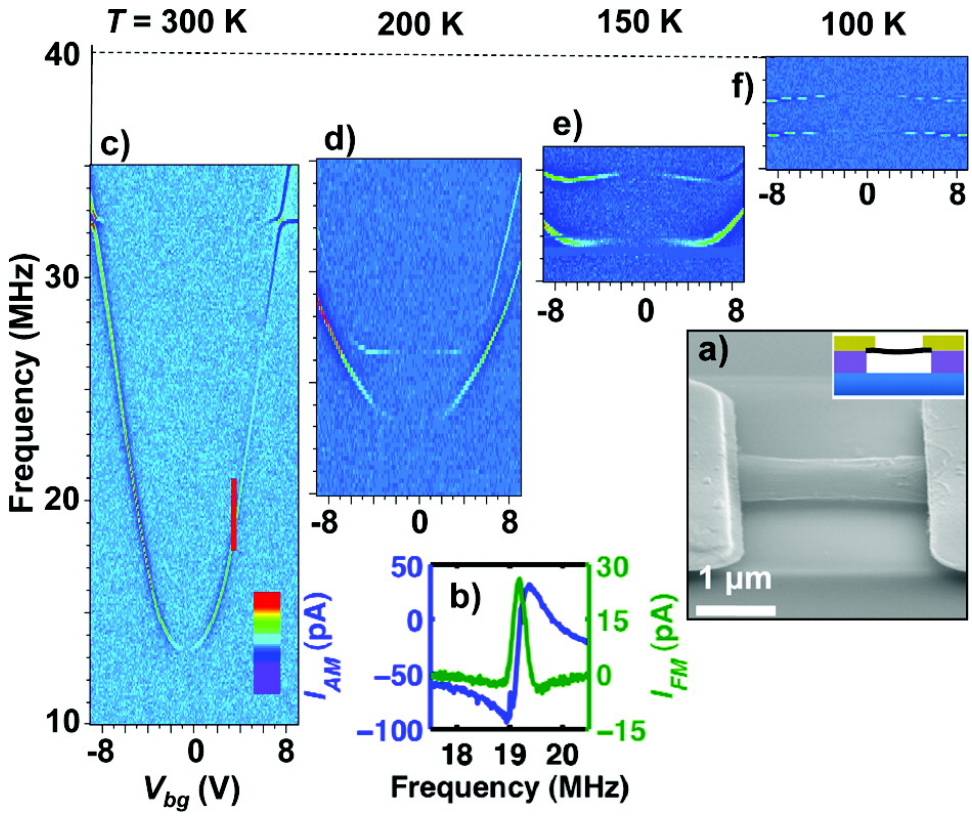

Figure 2.7: (a) Angled SEM image of suspended graphene clamped to gold electrodes with a degenerately doped silicon backgate. Schematic of cross-section inset. (b) Electrical mixing measurement of mechanical resonance of membrane shown in panel a versus frequency, measured using AM (blue) and FM (green) mixing techniques for $V_{bg} = 3$ V, $V_{rf} = 7$ mV. (c) FM mixing signal (colorscale spans -100 to 100 pA) versus gate voltage and drive frequency at room temperature. The resonance frequency is tuned by the electrostatic gate voltage. Red line indicates cut taken to get FM data shown in panel b. (d-f) The evolution of the tuning for the same resonator at $T = 200$, 150, and 100 K, respectively.

.

port measurements (see Supporting Information) show these devices have mobilities of $1000-4000\ \mathrm{cm}^2/\mathrm{V{\cdot}s}$, similar to previous results on CVD graphene [104, 121]. Using the electromechanical mixing measurement reported by Chen et al. [6], we actuated the resonators electrostatically and measured the motion using amplitude modulation (AM) [6, 119] or frequency modulation (FM) [127, 120] mixing. Figure 2.7b shows the electrical mixing response versus drive frequency for AM (blue) and FM (green) mixing techniques with back gate voltage $V_{bg} = 3$ V, and drive $V_{RF} = 7$ mV. Both techniques yield a resonator frequency $f_0 = 19.2$ MHz and quality factor of $Q = 44$ at this gate voltage.

Figure 2.7c shows the FM mixing current as a function of the drive frequency and electrostatic gate voltage at room temperature. The resonance frequency increases by more than a factor of 2 for large V_g and is symmetric around a minimum close to $V_g = 0$, very similar to the behavior previously reported for exfoliated graphene [6, 116].

Figure 2.7(d-f) shows the tuning of the same resonance at $T = 200$, 150, and 100 K. As the temperature is decreased the frequency of the resonator at $V_g = 0$ rises, while the dependence of the resonance frequency on V_g becomes weaker, and even reverses sign at 100 K. The change of frequency tunability with temperature is due to changes in the tension of the graphene as it is cooled and is similar to that seen in exfoliated graphene resonators [6, 116].

Figure 2.8 shows the inverse quality factor of a resonator versus temperature for a fixed $V_g = 3$ V. The inset shows the frequency versus temperature over the same temperature range. As the temperature is decreased, the quality factor rises dramatically from 150 at room temperature to 9000 at 9 K. This is comparable to the highest quality factors reported for graphene resonators at that temperature [6].

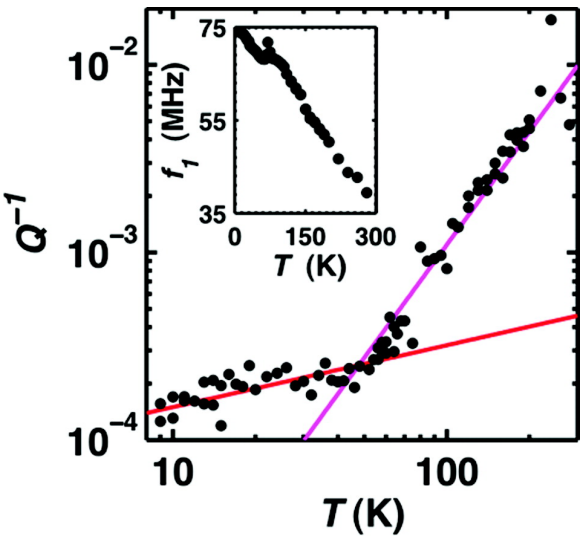

Figure 2.8: Inverse quality factor versus temperature at a $V_g = 3$ V; red and magenta lines show data scales as $T^{1/3}$ and $T^{2/3}$, respectively. Frequency versus temperature inset.

.

From Figure 2.8, the inverse quality factor scales approximately as T^{α} where $\alpha = 0.35 \pm 0.05$ from 9 up to 40 K, and as T^{β} where $\beta = 2.3 \pm 0.1$ from 40 K to room temperature. The temperature scaling is similar to what is found for exfoliated graphene resonators [6]. Similar temperature dependence is also seen in carbon nanotube resonators [128]. While there are many theories examining dissipation in these systems [129, 102, 130, 131, 132] the temperature dependence is still not well understood.

The techniques described here provide a step toward practical graphene-based devices. This work shows that it is possible to fabricate large arrays of low mass, high aspect ratio, CVD-grown single-layer graphene membranes while maintaining the remarkable electronic and mechanical properties previously observed for exfoliated graphene. This is an important conclusion, demonstrating that the benefit of wafer-scale processing allowed by CVD graphene comes at little or no cost in mechanical resonator performance.

Still, the data shown so far suggests that fabricating large arrays of supposedly identical doubly clamped beams does not mean that their properties will be uniform or that their dissipation will improve. In the next section, we will discuss how to solve these problems.

Chapter 3

Improved Quality Factor in Graphene Resonators

In this chapter, we demonstrate that the low room temperature quality factors observed in graphene resonators can be substantially improved using modern fabrication techniques. We find that for circular graphene drum resonators fabricated by chemical vapor deposition (CVD) methods, the quality factor is linearly dependent on the diameter of the resonator. We use this effect to produce resonators with Q as high as 2400 ± 300 at room temperature. These resonators have RQ products as high as 14,000 nm^{-1}, which rivals that of the best membrane resonators available today. Measurements of quality factor for different resonant modes suggest that Q is only weakly dependent on modal frequency and is determined predominantly by the size of the membrane. Together, these observations offer new insights into the dissipation mechanisms underlying graphene resonator performance. This chapter is adopted from [15].

3.1 Methods

Membranes such as the one shown in Figure 3.1a were fabricated following the procedure described in [9]. Graphene was grown on copper foil by chemical vapor deposition [104]. After a 30-50 nm thick layer of poly(methyl methacrylate) (PMMA) was spin-coated on the graphene to mediate transfer, the copper was dissolved in a ferric chloride-based etch (CE-200, Transene) and the graphene was rinsed in DI H_2O. Separately, a Si substrate coated with $\sim$ 300 nm thick Si-rich silicon nitride was back-etched using KOH to suspend a 2 mm $\times$ 2 mm square

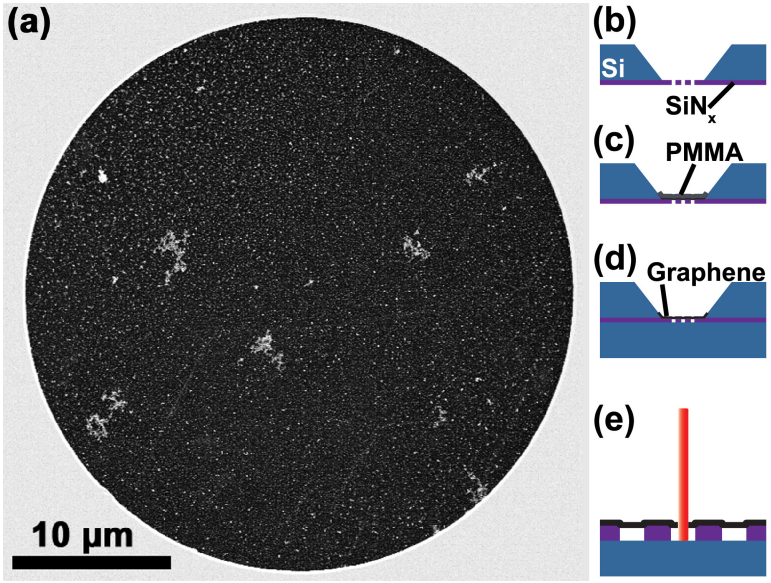

Figure 3.1: (a) SEM image of a suspended circular graphene membrane 30 μm in diameter. (b-d) Schematic of the fabrication procedure used to make the membrane in (a). Graphene on PMMA is transferred to a nitride membrane, the PMMA is decomposed, and the nitride is pressed flush against a polished silicon wafer. (e) Diagram of the interferometric apparatus used to detect resonator motion.

nitride membrane. Then, using photolithography, circular holes were patterned in the nitride membrane with diameter 2-30 microns (Figure 3.1). Following [104], the graphene was transferred to the backside of this substrate from the H_20 bath (Figure 3.1c). The graphene conformed to the substrate and adhered directly to the nitride membrane, covering many of the holes. After the graphene was allowed to dry in air, the PMMA was removed by decomposition at 350° C in air. This procedure resulted in suspended graphene drums with yields greater than 90% for holes 2 microns in diameter and as high as 25% for holes 30 microns in diameter. An example is shown in Figure 3.1a. We point out that localized contamination is visible on the surface of the graphene sheet. Transmission electron microscopy studies of graphene membranes prepared in an identical manner in Ref. [105] found that the bulk of the visible contamination was iron, oxygen, and carbon. However, the structural element of these resonators is monolayer graphene, as is evident from Raman spectroscopy.

Finally, we allowed the front side of the nitride wafer to adhere to blank piece of silicon. This step left graphene membranes up to 30 microns in diameter suspended on silicon nitride 300 nm above a silicon surface (see Figure 1d-e). Fixing the nitride membrane against the substrate was the crucial step that enabled us to measure quality factor in this work but not in the similar membranes of [9]. Surprisingly, we found no membranes that stuck to the silicon backplane as a result of this step.

In order to detect the resonance of the graphene drums, we used the interferometric method described in Section 2.3.2. Resonator motion is monitored by a HeNe laser reflecting from the resonator and the silicon backplane; the interference between these two reflections changes when the resonator moves and thereby changes the total reflected light intensity. These changes are monitored by a fast

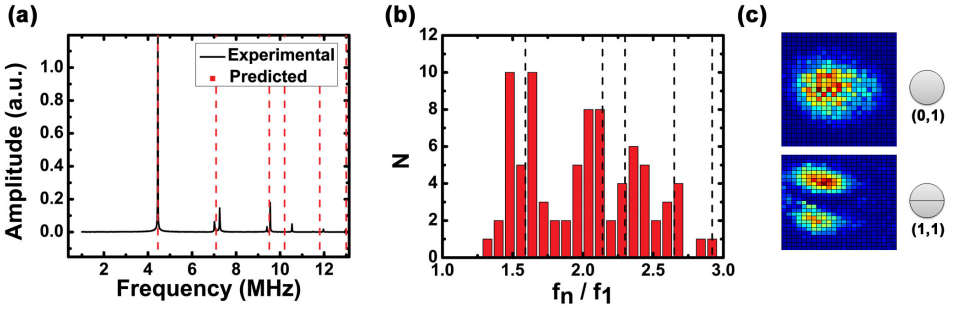

Figure 3.2: (a) Mechanical resonance spectrum for a circular graphene membrane (black) against the predicted location of all modes relative to the fundamental (red). (b) Histogram of the frequencies of all high order modes divided by the fundamental mode frequency for a set of 29 devices of various sizes. Black dotted lines show the expected frequency ratios for a circular membrane. (c) Amplitude of the resonance peak as a function of spatial position for the first two modes of a circular graphene membrane 22.5 μm in diameter. On gray circles, expected nodes for these modes are shown.

photodiode connected to a spectrum analyzer. Resonator motion is actuated using a 405 nm amplitude-modulated diode laser (Picoquant, Berlin, Germany) that excites motion through photothermal expansion and contraction of the graphene membrane. All resonance measurements were performed in a vacuum chamber evacuated to pressures less than 6×10^{-3} Torr, where viscous damping was found to be insignificant.

3.2 Results

We investigated both the spectra and fundamental modes of membranes of various sizes. As was shown in [9, 15], we found that clamping the membranes on all sides made the distribution of higher resonance modes relative to the fundamental modes predictable. A spectrum from one membrane that falls particularly close to a predicted spectrum is shown in Figure 3.2a. The dotted red lines show the

predicted frequencies of all modes given the fundamental mode of the membrane (modes are expected at 1.59, 2.14, 2.30, 2.65, and 2.92 times the fundamental frequency) [133]. Multiple peaks often cluster around the predicted frequency of a given mode, as for the second and third modes in Figure 3.2a. We attribute these peaks to theoretically degenerate modes whose degeneracy has been lifted by asymmetries in either the surface contamination or stress profile of the membranes. Figure 3.2b shows a histogram of the number of modes at a given multiple of the fundamental frequency for a set of 29 devices of various sizes; again, the peaks agree fairly well with theory. Measurements of the mode shapes of these circular membranes, obtained by measuring response amplitude as a function of laser position, confirm that the shapes of at least the first few modes are as predicted by the theory for circular membranes. Mode shape data for one membrane is presented in Figure 3.2c. This behavior should be contrasted with previous measurements of doubly clamped beam resonators made from exfoliated graphene, which frequently displayed complicated, unpredictable mode shapes [118].

In addition to the well-behaved spectra of these devices, we found that the fundamental frequency as a function of device size was well-described by a tensioned membrane model. In Figure 3.3a, we plot the fundamental frequency as a function of diameter for the set of 29 devices examined in Figure 3.2b. For circular membranes under tension, the fundamental frequency should follow [133]:

$$f = \frac{4.808}{2\pi D}\sqrt{\frac{Yt\varepsilon}{\rho\alpha}} \tag{3.1}$$

where D is the diameter, Yt is the in-plane Youngs modulus, ρ is the in-plane density of graphene, ε is the strain, and α is a density multiplier used to quantify the amount of mass contaminating the device ($\rho\alpha$ is defined to be the in-plane density of the resonator including both graphene and any additional mass). A

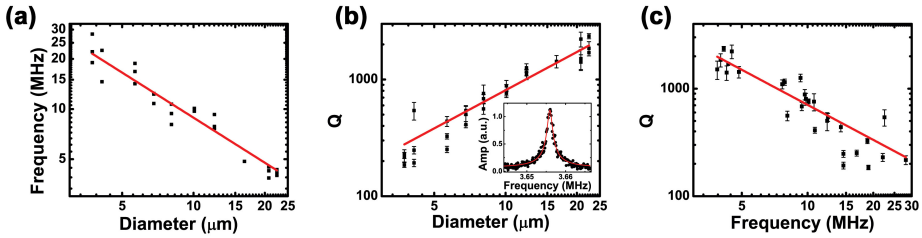

Figure 3.3: (a) Fundamental frequency f as a function of diameter D for the same set of devices studied in 3.2. The red line is a fit to the data revealing $f \sim D^{-0.9\pm0.1}$. (b) Quality factor of these graphene membranes as a function of diameter. The error bars represent the standard deviation in Q among 6 separate measurements of the width of the peak. The red line is a fit to the data revealing $Q \sim D^{1.1\pm0.1}$. Inset, the highest quality factor peak observed, with a Lorentzian fit revealing $Q = 2400 \pm 300$. (c) Quality factor as a function of frequency for the same devices plotted in (a) and (b).

fit of the data in Figure 3.3a shows that frequency is roughly proportional to inverse diameter as predicted by this equation. If we assume the known values for graphene, $Yt = 340$ N/m and $\rho = 7.4 \times 10^{-16}$ g μm^{-2}, we find that $\varepsilon/\alpha \sim 10^{-5}$. Since the density of the resonator is at least that of graphene ($\alpha > 1$), the minimum possible strain in the graphene is 10^{-5}, which is comparable to the strain in previously fabricated graphene resonators [4]. The tension is thought to be caused by the adherence of the graphene to the sidewalls of the nitride by van der Waals forces, a model supported by the consistency of the strain across many devices.

The quality factor of each device can be extracted from the full width half maximum of each Lorentzian resonance peak. A plot of the quality factor of fundamental modes as a function of diameter is shown in Figure 3.3b. There is a clear dependence of quality factor on resonator diameter, and fitting this data to $Q \sim D^{\beta}$ yields $\beta = 1.1 \pm 0.1$. The highest quality factor observed was 2400 ± 300

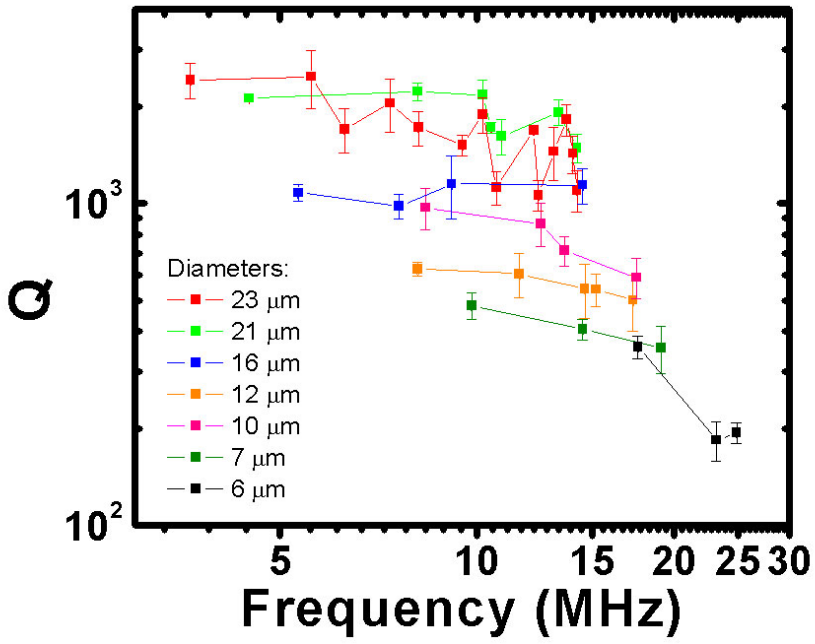

Figure 3.4: Quality factor as a function of modal frequency for resonators of different diameters. The dependence of dissipation on frequency is sublinear for all but the smallest resonator.

for a device with 22.5 μm diameter (Figure 3.3b, inset). We note that there was one 30 μm device measured in this data set, but it is not shown in these plots because it contained a significant rip. The quality factor of this ripped device was measured to be 1030 ± 150.

As a result of the dependence of both Q and frequency on diameter, Q must also be related to frequency, as shown in Figure 3.3c. To disentangle the effects of diameter and frequency on quality factor, we measure the quality factor of higher order modes of many membranes. Figure 3.4 shows the results of these measurements. With the possible exception of the smallest membranes, quality factor is not highly dependent on modal frequency. Certainly, the variation of Q with frequency between modes is less than linear for all but the smallest membrane. We therefore

surmise that size, rather than frequency, is the essential factor determining the Q of the membrane.

3.3 Mechanisms for Energy Loss

The origin of the dissipation in graphene resonators is currently unknown; however, the observations in the previous section provide some insight. We first discuss why we see high Q from the devices in this work and not for previously fabricated monolayer graphene doubly clamped beams, which have been studied as a function of length up to 6μm with no reported dependence on size [9]. Although the fabrication methods used here are less invasive than those used to fabricate doubly clamped beams from CVD graphene (the graphene here is exposed only to PMMA, copper etchant, and water), we do not believe that better treatment is responsible for the improved quality factor, since monolayer graphene resonators made by exfoliation, the cleanest possible method, also had low Q (~ 80) at room temperature [4]. More likely, the improvement in quality factor is due to fixing the membranes on all sides, which, according to simulations, improves Q by eliminating "spurious edge modes" [102]. The reproducible spectra of our membranes compared to those of doubly clamped membranes [9] lends further credence to this theory.

Even if fixing all sides of the membrane eliminates dissipation due to edge modes, we are confronting another source of dissipation that is dependent on size and not strongly dependent on modal frequency. We consider several candidate sources [129] of this dissipation in light of these observations. We find that the contribution from thermoelastic damping, which we calculate by treating the graphene as a clamped circular plate, is too small to be important for our resonators. The dependence of the dissipation on size, or, equivalently, perimeter to area ratio, suggests that anchor losses may play a role in graphene. However, a recent model

[134] of losses from phonon tunneling into the substrate gives dissipation estimates that are orders of magnitude too low, and it predicts a complicated behavior of quality factor as a function of mode that we do not observe here. A more probable candidate is surface related effects, which seem likely to play a role for these ultrathin resonators given the increase in dissipation of most NEMS with increased surface to volume ratio. We note that both the size dependence and the modal frequency dependence of circular graphene membranes are qualitatively similar to the dissipation in doubly clamped silicon nitride beams [135], which was found to be related to local strain in the resonators and possibly to coupling of the strain with surface defects [136]. Further modeling is required to examine these dissipation mechanisms. Measurements of the dissipation as a function of temperature should also prove revealing.

3.4 Comparing to Other Materials

To compare the dissipation in graphene to that in other mechanical resonators, we introduce a figure of merit known as RQ product. Liu et al. [10] introduced this figure of merit to account for the decrease in quality factor with increasing surface area to volume R, and it is a relevant measure of the performance of NEMS against the common problem of surface related losses. Taking the thickness of graphene to be 0.335 nm [137], the highest RQ product of a graphene resonator measured here is roughly $14,000$ nm^{-1}. In contrast, single crystal silicon nanomechanical devices [10] achieve at most RQ in the range $200 - 3000$ nm^{-1}.

It does seem clear, however, that high stress silicon nitride resonators have RQ products superior to those of graphene. Until recently, silicon nitride resonators had achieved RQ products of at most $80,000$ nm^{-1} for a 0.5mm $\times$ 0.5mm $\times$ 50nm square membrane [13]. However, new results from Adiga et al. suggest that even

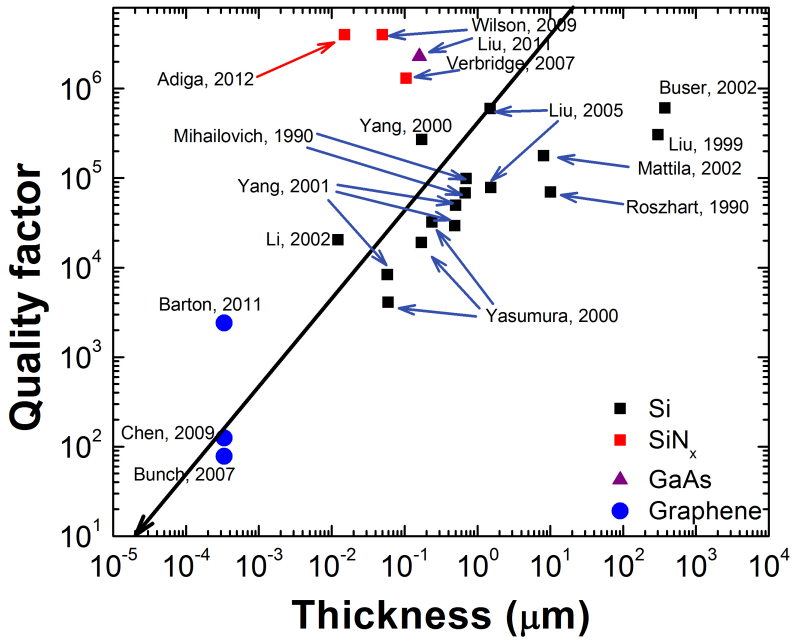

Figure 3.5: Room temperature quality factors for different materials [4, 10, 11, 12, 13, 14, 6, 15]. Solid line represents $RQ = 2000$ nm^{-1}.

very thin nitride resonators can have high quality factor. Specifically, a quality factor of 4.5 million was observed in a high-order radial mode for a drum resonator 700μm in diameter and 15 nm thick, corresponding to $RQ = 600,000$ nm^{-1}. Even adjusting for the fact that silicon nitride quality factors also seem to increase with increasing resonator size, it is clear that silicon nitride has a higher RQ product than graphene. However, this fact is likely due to the significantly higher strain in the nitride than in the graphene (further discussed in Chapter 4). See Figure 3.5 for a comparison of quality factors in silicon, silicon nitride, gallium arsenide, and graphene resonators.

The high RQ products observed here demonstrate that large graphene resonators have the potential to be very sensitive to mass per unit area. A com-

mercial quartz crystal microbalance can resolve approximately 400 pg cm^{-2}, while based on equation (1) and a study of the dynamic range achieved with our readout technique (see Supporting Information), a graphene resonator 12μm in diameter could resolve 3 pg cm^{-2} (4 attograms total mass). Further progress in biological functionalization should enable specific detection with this sensitivity, which would be useful for biomedical sensing. Also, the limit of force sensitivity for these resonators is $dF = (4k_{\text{eff}}k_BT/\omega Q)^{1/2}$, where k_{eff} is the effective spring constant, k_B is the Boltzmann constant, T is temperature, and ω is frequency. For our highest quality factor resonator, this limit is $dF \sim 200$ attonewtons / Hz$^{1/2}$, which is high for room temperature operation. Additionally, because $k_{\text{eff}} \sim m_{\text{eff}}\omega^2$ is independent of diameter, and because we find empirically that ωQ is independent of diameter, this limit of force sensitivity is independent of the resonator area. Therefore, large-area graphene membrane resonators should enable very sensitive measurements of force per unit area.

This study provides information about dissipation in monolayer graphene resonators that was not accessible before the recent advances in graphene fabrication. We show that quality factor in tensile graphene drums is proportional to the diameter of the membrane. For our largest resonators, we observe RQ products as high as $14,000$ nm^{-1}. It therefore appears that relative to its low mass, graphene offers an excellent quality factor in addition to its high frequency and high electrical conductivity, making it an ideal material for NEMS.

Chapter 4

Further Improvements in Quality Factor

4.1 Introduction

As mentioned previously, NEMS composed of silicon nitride have the highest known quality factor relative to their thickness [135]. However, their quality factor is known to be enhanced by extremely large stress. Consider, for example, the devices discussed in [138], which have an inherent tensile stress of 1200 MPa corresponding strain of $\epsilon \approx 0.6\%$. To put this number in perspective, the graphene drums in the previous chapter had an estimated tensile strain of at least $\epsilon \sim 10^{-5}$. Since the total energy is proportional to stress σ_0 (shown below for a doubly clamped beam with width w, height h, and displacement $u_m(x)$):

$$E \approx \frac{1}{2}\int_L dx w h \sigma_0 \left(\frac{\partial}{\partial x} u_m(x)\right)^2$$

and quality factor is proportional to E (see Eq. 1.5), this means that quality factor is proportional to strain. Thus it should be possible to further improve the quality factor of graphene by adding stress. Indeed, since graphene is the world's strongest material [139], it ought to be capable of strain on the order of $\epsilon \approx 10^{-1}$, leaving up to four orders of magnitude of potential Q enhancement for the devices shown in the previous chapter.

For this reason as well as others, methods to add strain to graphene resonators are desirable for NEMS applications. Below, we will discuss our efforts in strain engineering of graphene. We will also present our efforts to make graphene/nitride hybrid devices that exploit the high quality factors of silicon nitride while adding graphene's beneficial electrical properties. Ultimately, this research could lead to extremely thin resonators with useful combinations of mechanical and electrical

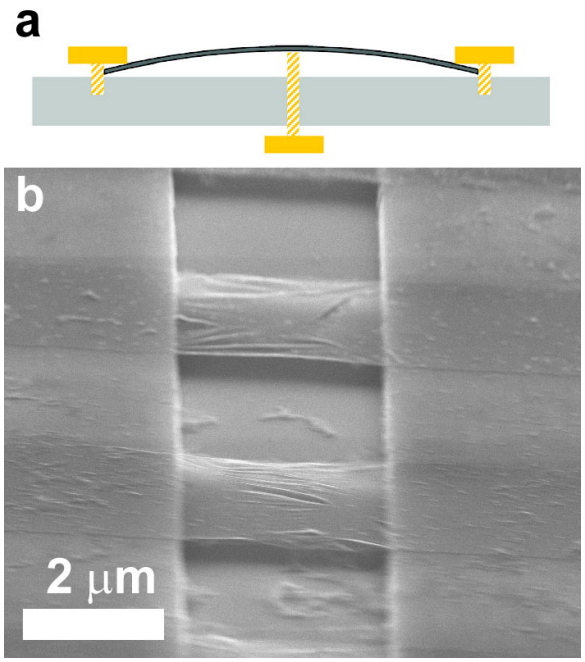

Figure 4.1: (a) The setup used to stretch graphene on SiO_2 and Si. Two screws hold the silicon chip in place while a third screw bends the chip from underneath. Reproduced from [12]. (b) CVD graphene devices across trenches in SiO_2 with length $\sim 2\mu$m were stretched.

properties.

4.2 Stretching Graphene

Strain engineering of graphene has been successfully accomplished before using thermal expansion [140]. However, to understand the role of strain independent from other variables, more direct control of strain is desirable. We attempted to discover the effects of strain on quality factor by fabricating graphene on a flexible substrate and bending the substrate to induce tension. This method is identical to that used for establishing the link between strain and quality factor of silicon nitride [12]. A schematic is shown in Figure 4.1.

To simplify the fabrication, we began by simply using silicon with SiO_2 trenches

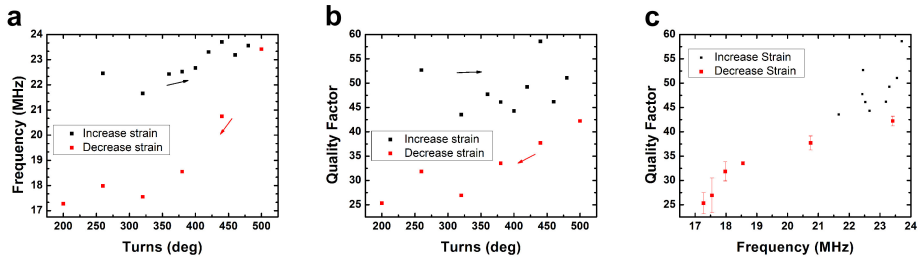

Figure 4.2: (a) Stretching of a graphene doubly clamped beam on SiO_2 like those shown in Figure 4.1b. The black points represent increasing applied strain; the red points represent decreasing applied strain. The lack of change in frequency during increasing applied strain implies that the graphene is slipping on the substrate. (b) Quality factor as a function of chip bending during the same experiment as (a). (c) Quality factor as a function of frequency for the same experiments; quality factor is clearly correlated with frequency.

as the substrate (Figure 4.1b). This approach suffered from the fragility of the silicon chip, which broke easily when it was strained. However, we did obtain preliminary data shown in Figure 4.2. As can be seen from Figure 4.2a, turning the screw to increase applied strain did not significantly change the frequency, while decreasing the applied strain seemed to lower the frequency substantially. This phenomenon can be explained as follows: when strain is increasing, the graphene slips on top of the SiO_2 because the adhesion to the SiO_2 is insufficient to hold it in place (a similar phenomenon was reported in [140]). When the tension is relieved, slack is introduced to the beam and frequency drops. As can be seen from Figures 4.2b-c, quality factor is closely related to frequency. It is difficult to increase quality factor above the as-made value because the slipping does not permit high strains, but it is easy to decrease quality factor by introducing slack into the beam. This data provides good experimental evidence for our hypothesis that graphene's quality factor is proportional to stress.

We tried to improve on this first attempt by creating a more flexible sub-

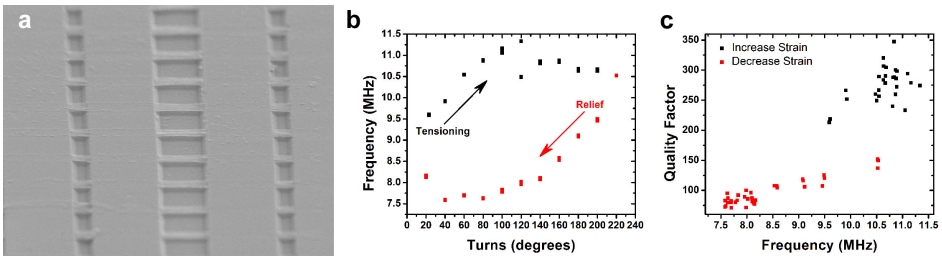

Figure 4.3: (a) Graphene suspended on Zeonor plastic. (b) Frequency as a function of turns of the screw to bend the Zeonor. The flattening of frequency with increasing turns of the screw is evidence of slipping. (c) Quality factor as a function of frequency for graphene stretched on Zeonor.

strate that would not break during chip bending. First, we attempted to fabricate graphene on suspended on trenches in PDMS. This effort, however, was futile, because graphene on an elastic substrate will simply deform the substrate until it conforms to the substrate's topography [141]. No suspended monolayers could be fabricated on top of PDMS. Next, we used Zeonor plastic as the flexible material, which had the advantage of resistance to chemicals capable of removing PMMA after graphene transfer. We fabricated trenches $\sim 500\mu$m deep in Zeonor plastic using a patterned silicon wafer as a mold [142]. We then transferred graphene to the substrate using acetone to dissolve the PMMA. The resulting doubly clamped graphene beam devices are shown in Figure 4.3a.

We added tension to the graphene-on-Zeonor devices using the chip bending method and monitored the resonance frequency using standard interferometric techniques. The results for a 5μm device are shown in Figure 4.3b-c. This time, when tension is increased the frequency appears to increase and then level off, while when the tension is decreased the frequency falls immediately in a hysteretic path. Quality factor appears to rise slightly in response to the initial tensioning, but it appears that again the quality factor is limited by slipping between the Zeonor

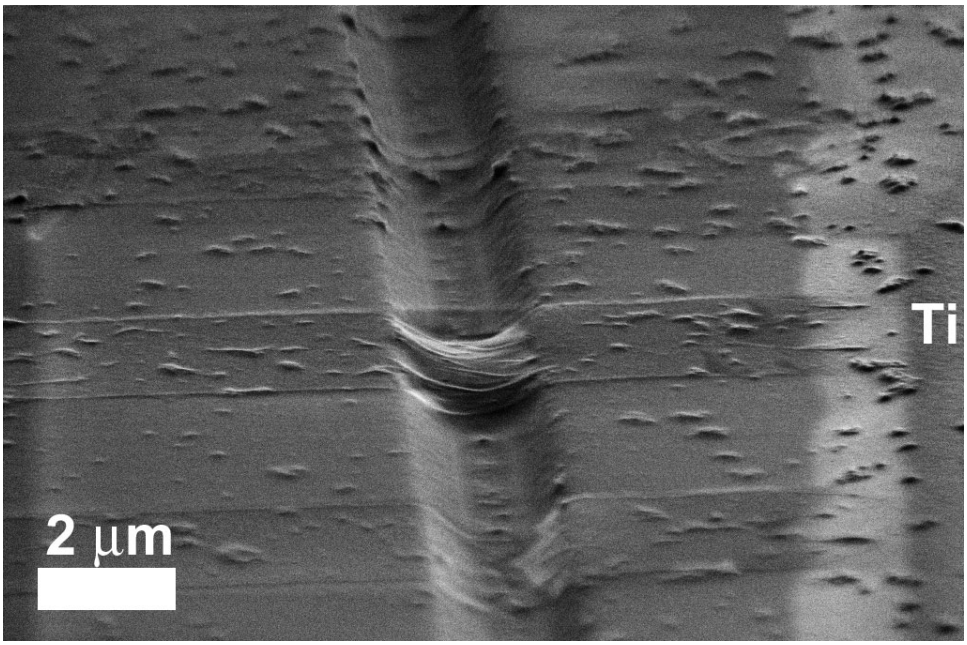

Figure 4.4: Doubly clamped beams with titanium clamps after a stretching experiment. It appears that the graphene still slipped during stretching, introducing slack. Evidence of tearing is present at multiple points.

and the graphene.

We attempted to address the slipping issue by using a shadow mask to put down Ti "clamps" on either side of the doubly clamped graphene beams. Stretching graphene "clamped" in this way did not yield improvements in quality factor compared to the as-fabricated devices. When the devices were examined in SEM following the chip bending experiment, evidence of slipping and some evidence of tearing was observed (see Figure 4.4). It is likely that our clamps were either ineffective in adhering to the graphene or that the graphene simply tore away from the clamp. These efforts were likely hindered by the weak strength of graphene at grain boundaries [107] or additional weaknesses introduced by patterning. Stretching large-grain graphene membranes with circularly symmetric strain might overcome these difficulties and enable further progress.

4.3 Graphene on Nitride

Another way to take advantage of strained materials to improve the mechanical properties of graphene is to put the graphene on top of an already-strained material, such as silicon nitride. The graphene's negligible thickness will ensure that the energy stored in the two-material resonator during vibration remains high. As long as the graphene does not provide additional dissipation channels, the overall device should retain the high quality factor possessed by the original material.

We investigated this idea by fabricating graphene/nitride hybrid devices consisting of suspended nitride mechanical resonators covered by one monolayer of CVD graphene. We tried several different fabrication methods with varying success. The first method began with a stack of nitride on SiO_2 on Si, onto which we transferred a uniform layer of CVD graphene. Then, we patterned doubly clamped beams into the graphene and nitride using an O_2 plasma to etch the graphene and CF_4 to etch the nitride. Finally, BOE was used to remove the oxide. We found that this approach usually resulted in flawed devices because the BOE tended to lift the graphene away from the nitride substrate.

One way to avoid damage of the graphene by the release etchant is to put the graphene down after the structure is released. However, to do this with doubly clamped beams is very challenging, because the graphene would have to be patterned and transferred to fall only on top of the beams. One solution is to change the geometry of the resonator - for example, if a 2D fully clamped nitride membrane resonator were used, large-area graphene could simply be transferred on top. We accomplished this by using devices like those discussed in Ref. [143, 144]. Following HF release of the membranes from their underlying oxide layer, graphene was added to the top of the nitride using a dry transfer technique similar to that discussed in [145]. Images of the resulting devices are shown in Figure 4.5.

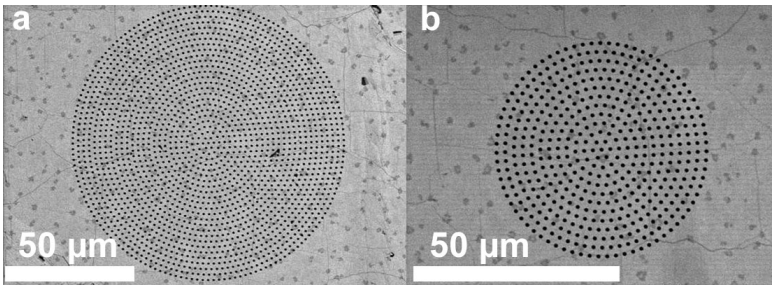

Figure 4.5: Scanning electron micrographs of graphene on nitride drum resonators. The resonators appear as a circle of release holes that have allowed BOE to etch all oxide from beneath the circle. The entire field of view is covered by graphene, which is identifiable by the folds that cross the resonators and by the small (several micron) patches of bilayer graphene that appear darker than the surrounding area.

We examined the mechanical properties of these hybrid resonators using the standard optical resonance techniques. We were primarily interested whether the presence of graphene would diminish the quality factor of these membranes. Data for as-fabricated circular nitride membranes is presented in Figure 4.6a, while data for a different set of circular nitride membranes is presented in Figure 4.6b. It appears that the quality factor is virtually unchanged by the presence of the graphene, since resonators with similar diameters have similar dissipation regardless of the presence of graphene. These results are preliminary and a more careful experiment would investigate the same resonator before and after deposition of graphene. These experiments are now ongoing.

It is intriguing that the graphene seems to provide a very weak channel of dissipation, despite the fact that the earliest graphene resonators had extremely low quality factor. This data supports the picture that emerges from Chapter 3 and other work that graphene itself is not excessively dissipative, but that the stored energy in the resonators is simply small relative to the defects that often emerge in their fabrication.

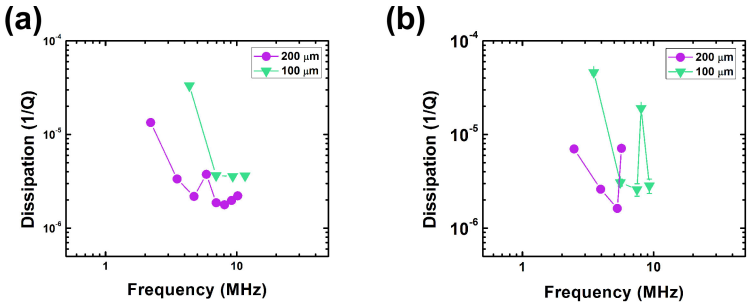

Figure 4.6: (a) Nitride membranes of varying diameters and thickness $\sim$ 75 nm. (b) Nitride membranes of unknown thickness less than 75 nm covered with one monolayer of CVD-grown graphene. In both figures, purple dots represent 200 μm diameter; green dots represent 100 μm diameter. Quality factor appears virtually unchanged when the monolayer of graphene is added.

Chapter 5

Optomechanics of Graphene Resonators

By virtue of their low mass and stiffness, atomically thin mechanical resonators are attractive candidates for use in the thriving research field of optomechanics. In this chapter, we explore the potential applications for graphene in optomechanics. We find that the best means of achieving optomechanical coupling to a graphene resonator may be through photothermal rather than radiation pressure forces, and we demonstrate photothermal back-action in a graphene mechanical resonator comprising one end of a low-finesse Fabry-Perot cavity. As a demonstration of the utility of this effect, we show that a continuous wave laser can be used to cool a graphene vibrational mode or to power a graphene-based tunable-frequency oscillator. By virtue of graphene's high thermal conductivity and optical absorption, photothermal optomechanics is efficient in graphene and could ultimately enable laser cooling to the quantum ground state or applications such as photonic signal processing. Much of this Chapter is reproduced from [146].

Optomechanics [1, 38] which uses optical feedback and other back-action forces to control mechanical elements, has generated much interest since it was applied to micro- and nanomechanical systems [44]. Research in optomechanics has largely focused on using back-action to cool mechanical modes of mesoscopic resonators to their quantum ground state, with progress first shown using photothermal forces in metal-coated cantilevers [46], and later demonstrated using radiation pressure forces on mirrors [47, 48, 49], membranes [147], and strings [148]. Many other potential applications have also emerged, such as force sensing [40], non-volatile mechanical memory [41], and photonic signal processing [42, 43]. For all of these applications, it is desirable to have a mechanical resonator with low mass and

therefore low stiffness $K = m\omega^2$ in order to improve the sensitivity of the structure to the forces of light. There are additional benefits associated with low stiffness; for example, it allows for cavity tuning of optical resonance for filters, and it increases the amplitude of zero-point motion $x_{zp}^2 = \hbar\omega/K$. As a result, the drive to reduce the size of the mechanical elements has been an important enabling factor for recent milestones such as optical cooling of a resonator to the quantum ground state [52]. Ideally, the mechanical element would be reduced to the limit of atomic thickness, but such a resonator would need to have both good mechanical properties and strong coupling to light, which is challenging for such a small object.

Graphene, a single layer of carbon atoms in a hexagonal lattice, is uniquely poised to meet these challenges. Mechanical resonators made from graphene [4, 15, 6, 116] are simple to fabricate [9], benefit from graphene's high strength and Young's modulus [139], and have demonstrated frequencies as high as 178 MHz [149], with quality factors of up to 2,400 at room temperature [15] and 100,000 at 100 mK [150]. Already, graphene resonators have been applied as excellent sensors of mass [6] and force [116], and they are capable of RF electrical readout for signal processing applications [112]. At the same time, graphene's optoelectronic properties ensure a strong ($\pi\alpha = 2.3\%$), constant absorption of light across a wide range of wavelengths [151, 113]. Studying optomechanical coupling resulting from this absorption could shed light on photothermal processes in graphene [152], with applications in e.g. bolometry [153]. Optomechanical back-action cooling of graphene is also expected to be useful, since the relatively high zero-point motion and frequency of graphene resonators makes them ideal [31] for pursuing the quantum regime [36, 52, 51]. Despite graphene's advantages, no mechanism for optomechanical back-action coupling to these membranes has been demonstrated.

We investigated the optomechanical behavior of a graphene resonator forming

one end of a low-finesse Fabry-Perot cavity. We found strong photothermal coupling between the light and the graphene leading to optical back-action that can be used to cool the graphene (i.e., reduce its thermal motion) or to counter the mechanical damping of a resonant mode, inducing self-oscillation. Our graphene optomechanical resonators have fundamental flexural mode effective masses as small as $m_{eff} \approx 100$ fg, comparable to that of the smallest optomechanical systems demonstrated to date [154] and nearly two orders of magnitude lower than that of other electrically integrated optomechanical systems [155]. In contrast with other systems that have demonstrated similar photothermal effects [44, 46, 156], graphenes low stiffness in combination with strong electrostatic coupling enables tuning of the resonant frequency by more than 100% over 15 V [6]. Strong electrostatic mechanical frequency tunability is a novel feature for optomechanical systems and will be useful for applications in signal processing, while the low stiffness of graphene at relatively high frequencies makes graphene optomechanical systems relevant for the pursuit of mechanical systems in the quantum regime.

5.1 Methods

5.1.1 Experimental Setup

The resonators used for this experiment are suspended single layer graphene. They are clamped on all sides to a silicon dioxide substrate and electrically contacted with source, drain, and gate electrodes (Figure 5.2). The resonators were batch-fabricated from CVD graphene [9] following procedures detailed in Section 5.1.2. The gap between the graphene and the metal gate acts as an optical cavity from which the reflectivity R is dependent on the displacement z of the graphene toward the backplane. To monitor mechanical resonance, a continuous wave (CW)

laser impinges on the cavity and reflected laser light is modulated by an amount proportional to $\Delta z(\omega) dR/dz$, where $\Delta z(\omega)$ is the amplitude of the vibration at a given frequency ω. The reflected light is monitored by a fast photodiode connected to a network analyzer. Motion is actuated capacitively by applying a modulated voltage V_g between the graphene and the gate. The graphene device is placed inside of a vacuum chamber in which the pressure is less than 10^{-6} Torr. We present results for two devices, a suspended square of graphene ("Device 1") and a suspended circle of graphene ("Device 2").

5.1.2 Fabrication

The procedure for fabricating devices was based on an earlier article [9]. Fabrication began with the thermal growth of 240 nm SiO2 on a 10 kΩ·cm Si wafer. Trenches were patterned in the SiO_2 / Si using photolithography followed by reactive ion etching. Etching of the trenches consisted of two steps: first, a directional CHF_3 / O_2 or CF_4 etch was used to etch the SiO_2 and Si; then, an isotropic SF_6 / O_2 etch was used to create an undercut profile in the Si beneath the oxide ($\sim$ 200 nm undercut). The undercut was designed to prevent shorting between the source/drain and gate electrodes during the following metal evaporation step. After the etch, an additional 220 nm of oxide was thermally grown. Next, source, drain, and gate electrodes were patterned in a single photolithography step, followed by e-beam evaporation of 5 nm Ti / 25 nm Pt.

Graphene was grown by CVD on copper foil and transferred using the method developed by Li et al. [104]. To make Device 1, graphene on Cu foil was patterned into 50μm $\times$50μm squares using photoresist and contact lithography followed by O_2 plasma etching ([9]). The resist was removed by sonication in Microposit Remover 1165 (n-methyl-pyrrolidinone), and 4% 495k MW poly(methyl methacry-

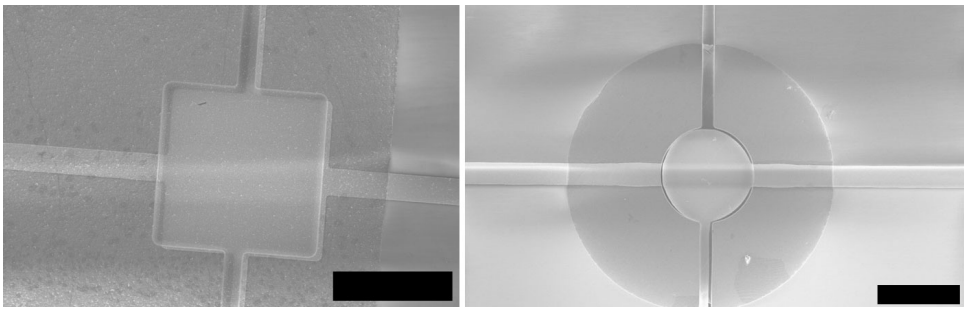

Figure 5.1: Device 1 (left) and Device 2 (right). Scale bars are 10μm. Graphene is suspended over a square (Device 1) or circular (Device 2) trench in SiO_2. An additional trench extends vertically from the top and bottom of each square/circular trench to allow liquid to drain from beneath the graphene after transfer. Platinum source and drain electrodes contact the graphene from the underside. A gate electrode lies along the bottom of each trench.

late) (PMMA) in anisole was spun onto the surface of the graphene/copper. The copper was etched in ferric chloride; the graphene was rinsed by transferring it to several water baths and finally transferred to the substrate. The squares of graphene landed randomly in this procedure. The PMMA was removed in dichloromethane, and the devices were rinsed in IPA and critical point dried to prevent stiction.

Device 2 was patterned using a novel procedure designed to improve yield. Graphene grown on Cu foil was transferred directly to the substrate using PMMA as the support layer as described above. Importantly, however, after spinning PMMA onto the graphene on Cu foil, the foil was baked on a hotplate at 170°C for 5 minutes. After transfer, a layer of Shipley 1813 resist was spun on top of the PMMA and the resist was patterned using optical lithography. Then, oxygen plasma was used to etch the pattern into the PMMA and graphene. Finally, the resist and PMMA were both removed using Microposit Remover 1165. The chip was transferred to IPA and critical point dried.

Device properties are listed in the table below. The density ρ and initial tension σ_0 are determined by fitting frequency as a function of gate voltage, as described in Appendix B. All other data are measured experimentally. We measure the distance d between the graphene and the electrode in the absence of a gate voltage using an optical profilometer. We measure the length L along the side of Device 1 and the radius a of Device 2 from SEMs. Images of both devices are shown in Figure 5.1.

Device	Dimensions (μm)	d (μm)	ρ/ρ_g	σ_0 (N/m)
1	$L/2 = 7.0 \pm 0.1$	1.96	4.6 ± 0.3	0.013 ± 0.001
2	$a = 5.5 \pm 0.1$	1.37	2.9 ± 0.2	0.010 ± 0.001

5.2 Results

We characterize the resonators by driving their motion capacitively and optically monitoring their response at low laser powers, where optomechanical effects are minimized. Amplitude of motion as a function of frequency and gate voltage for Device 1 is shown in Fig. 5.3a. Previous work [6, 116] has shown that the shape of the frequency as a function of gate voltage can be used to extract the destiny of the resonator. For Device 1, the areal density is $\rho = 5 \times \rho_{\text{graphene}}$ corresponding to a total device mass of $m = 700$ fg ($m_{\text{eff}} \approx 200$ fg assuming that the contaminating mass [6, 15] is evenly distributed). For Device 2, the same calculation gives $\rho = 3 \times \rho_{\text{graphene}}$ and $m = 200$ fg ($m_{\text{eff}} \approx 100$ fg). At a given gate voltage, amplitude versus frequency curves (Fig. 5.3b) fit well to a Lorentzian, allowing us to extract the fundamental frequency ω_0, the full width half maximum (FWHM) Γ, and the quality factor $Q = \omega_0/\Gamma$.

As CW laser intensity is increased, we find that the damping as measured by the FWHM depends on laser power. For laser wavelength $\lambda = 633$ nm, the effective

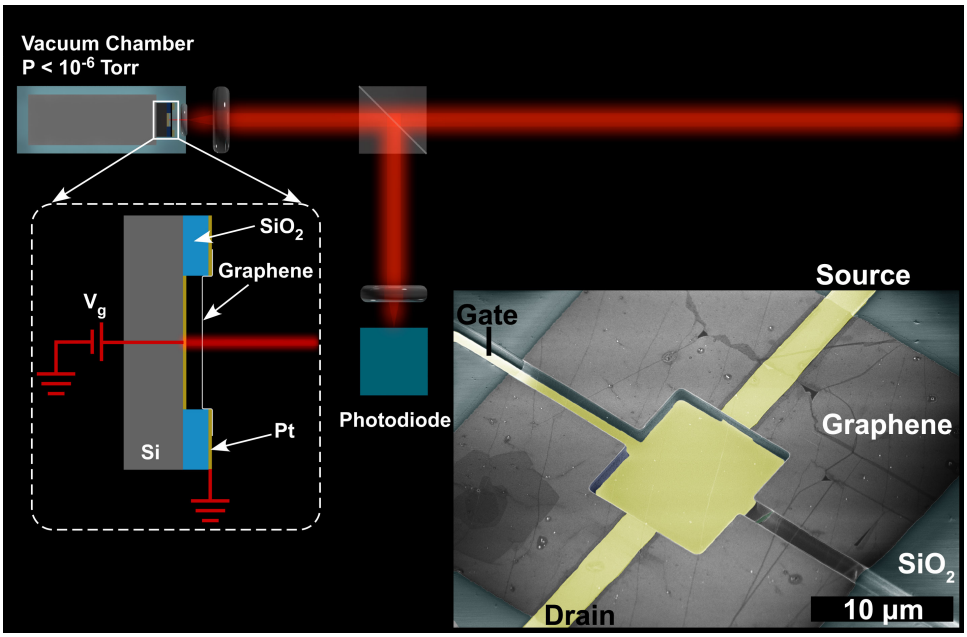

Figure 5.2: Experimental setup. A laser at either visible or IR wavelengths reflects from the cavity formed between the graphene and the platinum backplane; variations in the reflected laser light are monitored by a photodiode. A gate voltage Vg is applied between the graphene and the underlying electrode; this voltage is sometimes modulated for measurements of driven motion. Inset, a false-color SEM of a typical graphene membrane resonator.

damping Γ_{eff} increases linearly with power (Fig 5.3d), whereas at $\lambda = 633$ nm, Γ_{eff} decreases linearly with power (Fig 5.3e). The dependence of the effect on both power and wavelength demonstrates that the damping is the result of an interaction with the optical cavity. According to the theory for optomechanical coupling to a low-finesse cavity, if there is a light-induced force F on the membrane that acts with time delay τ, such as radiation pressure or a photothermal force, the effective damping Γ_{eff} should follow [56]:

$$\Gamma_{\text{eff}} = \Gamma \left(1 + Q \frac{\omega_0 \tau}{1 + \omega_0^2 \tau^2} \frac{\nabla F}{K} \right) \tag{5.1}$$

where $\nabla F = dF/dz$. The difference in the sign of the optomechanically induced damping $\Gamma_{OM} = \Gamma Q \frac{\omega_0 \tau}{1+\omega 0^2 \tau^2} \frac{\nabla F}{K}$ between $\lambda = 568$ nm and $\lambda = 633$ nm is consistent with an effect in which the force is proportional to the optical energy flux absorbed by the graphene $W_a(z)$; calculations (Appendix A and Fig 5.3c) show that dW_a/dz has a different sign for $\lambda = 568$ nm and $\lambda = 633$ nm. The frequency shifts over the same range are dominated by the static change in membrane tension from laser heating (Section 5.3.4).

The electrostatic gate voltage can be used to tune the optical properties of the cavity, as shown in Fig 5.4 for Device 2. In Fig. 5.4a, the mechanical resonant frequency is usually visible as it tunes with gate voltage. However, at $V_g \approx \pm 4.3$ V, the signal vanishes because the membrane is at a maximum of reflectance where dR/dz changes sign. Because dR/dz and dW_a/dz change sign simultaneously (Fig. 5.3c), we expect that the sign of Γ_{OM} should also differ depending on whether $|V_g| < 4.3$ V. Indeed, we find that at $V_g = -10$ V, Γ_{OM} is negative (Fig. 5.4c), while at $V_g = 2$ V, Γ_{OM} is positive (Fig. 5.4d). Therefore, at a fixed wavelength $\lambda = 532$ nm, the sign of the optomechanical damping can be controlled by electrical cavity detuning.

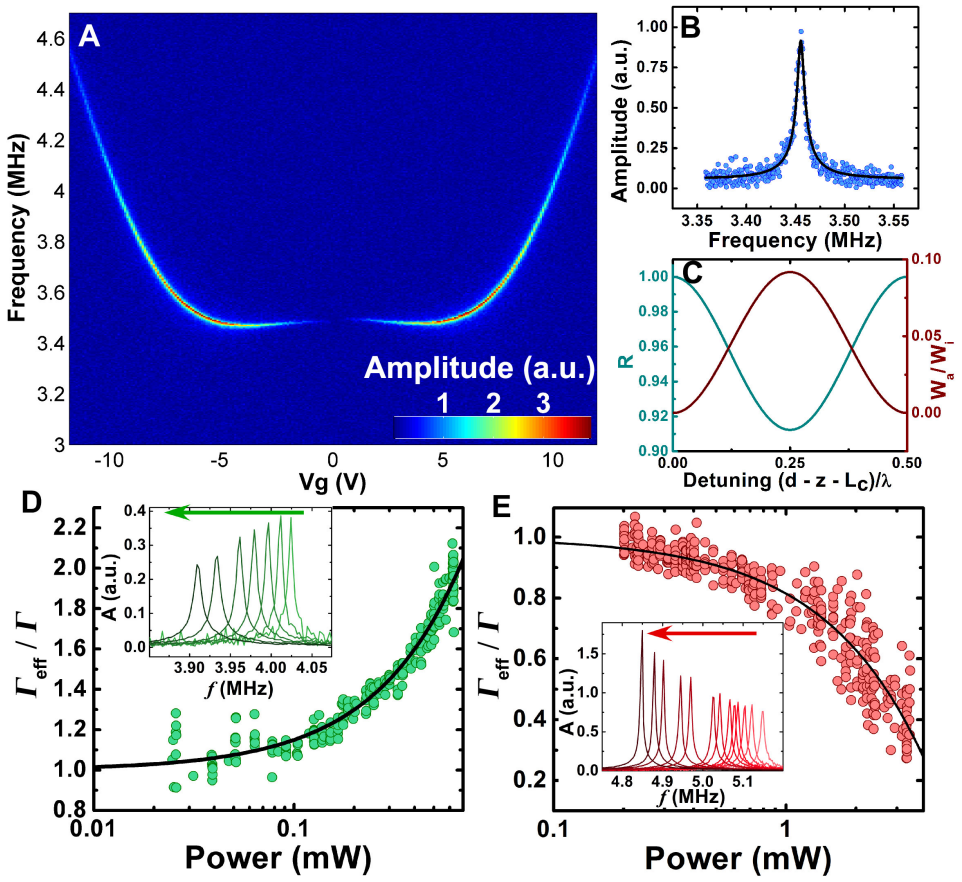

Figure 5.3: (A) Amplitude of the reflected light as a function of frequency and gate voltage for Device 1 at low laser power ($300\mu W$). (B) Amplitude as a function of frequency at $V_g = 5$ V from (A) is fit to a Lorentzian, yielding $\omega_0 = 2\pi \times 3.46$ MHz, $\Gamma = 2\pi \times 6800$ Hz, and $Q = 500$. (C) Calculated cavity reflectivity R and graphene absorbed energy flux W_a normalized by the incident energy flux W_i as a function of detuning from the resonant cavity length L_c. For the cavity length of Device 1, $(d - L_c)/\lambda = 0.45$ for $\lambda = 568$ nm, and $(d - L_c)/\lambda = 0.10$ for $\lambda = 633$ nm; the change in sign of dW_a/dz leads to opposite optomechanical damping in (D) and (E). (D) Damping increases as a function of CW laser power ($\lambda = 568$ nm) for capacitively driven graphene resonance. (E) Damping decreases with CW laser power ($\lambda = 633$ nm) for capacitively driven graphene resonance. For (D-E), the data is plotted on a semi-logarithmic scale to clearly show a broad range of powers; black lines are fits to a linear dependence of Γ_{eff}/Γ on power. Insets show amplitude versus frequency plots; red and green arrows represent increasing powers.

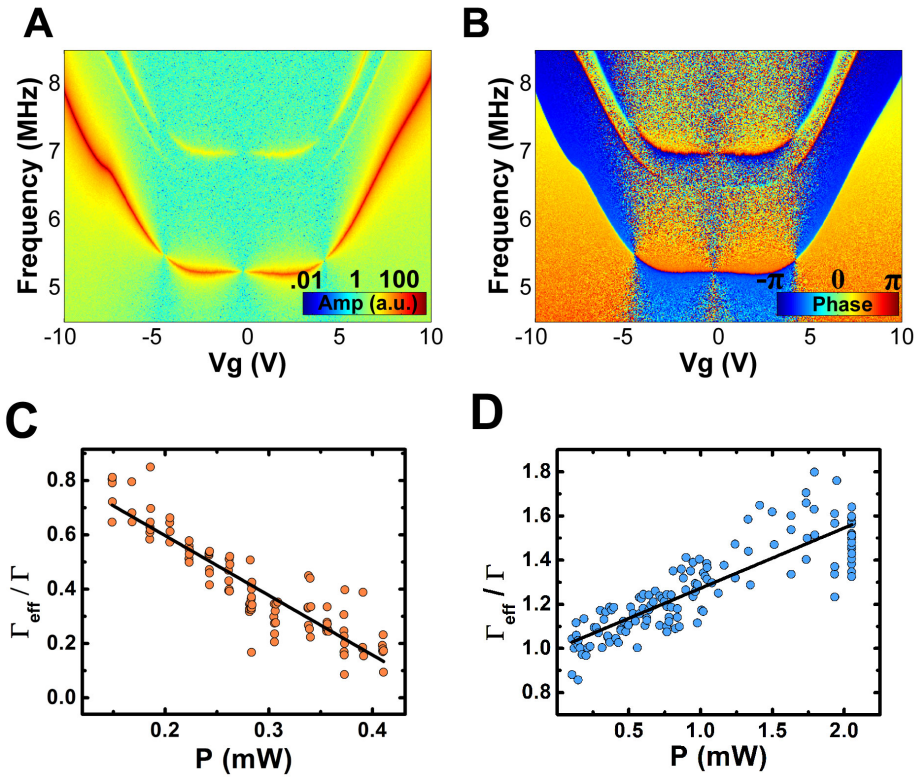

Figure 5.4: (A) Log-scale amplitude as a function of frequency and Vg for Device 2 ($\lambda = 532$ nm, $P = 500\mu W$). (B) The phase of the signal relative to the electrical drive as a function of $\omega/2\pi$ and V_g. The phase shift noticeable as a change in color at a given frequency at ± 4.3 V indicates that dR/dz has changed sign. The sign of dW_a/dz changes simultaneously. (C) Measurements at $V_g = -10$ V show that damping decreases with laser power (Γ_{OM} is negative). (D) Measurements at $V_g = 2$ V show that damping increases with laser power (Γ_{OM} is positive).

5.3 Modeling

5.3.1 Overview

The observed optomechanical effects can be understood using a 2D model for a circular drumhead resonator. The feedback observed here requires that the motion of the membrane induce a force that acts on the resonator parallel to the direction of motion and with some time delay. Candidates include photothermal forces and radiation pressure. First, we calculate how such a force could arise from photothermal effects; that is, changes in tension of the membrane due to laser-induced heating. In order to explain how tension could provide a force in the z-direction, we consider the case in which the center of the membrane is displaced by an initial amount z_0, leading to a contact angle θ_0 between the plane of the chip and the membrane [156]. Such a displacement must arise, for example, from a DC gate voltage. In this case, a component of the photothermal force acts along the direction of motion z (see Section 5.3.2), causing a photon-induced rigidity

$$\nabla F_{pth} = AP\frac{4\pi^2 a}{\lambda}\sin(\theta_0)sin\left(\frac{4\pi}{\lambda}(d-z_0)\right) \tag{5.2}$$

where a is the radius of the membrane, λ is the laser wavelength, P is the incident laser power, and d is the distance of the membrane from the gate in the absence of gate voltage. The proportionality constant A indicates how much the tension in the membrane changes with incident laser power. We obtain A empirically by using the frequency shift with increased laser power at $V_g = 0$ as a measure of laser-induced stress; we find $A = 15$ N/(m $\cdot$ W), in reasonable agreement with the value expected from thermal expansion (see Section 5.3.3). Estimating τ and θ_0, we find that the predictions of Eqs. 1 and 2 agree to within approximately an order of magnitude with the results observed in Fig. 5.4 d-e. We also consider the possibility of an optomechanical effect from radiation pressure, but the force is

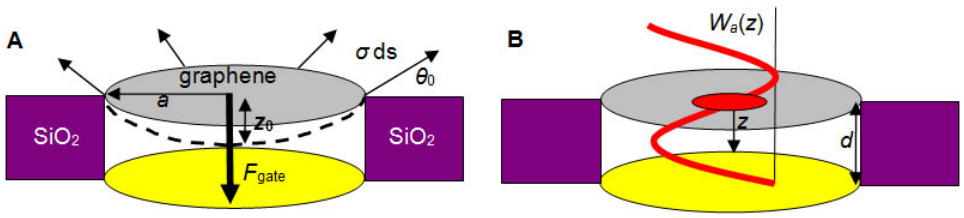

Figure 5.5: (A) Schematic of the model used to find the equilibrium position of the graphene membrane as a function of gate voltage. (B) Schematic showing the energy density in the electric field produced by incident light. The absorbed power $W_a(z)$ is proportional to the energy in the electric field. The photothermal spring constant is proportional to the gradient of the field.

too weak to affect either the frequency or the damping of the graphene resonators. Additionally, we study the dependence of Γ_{OM} on both λ and V_g and find that it agrees with Eq. 5.2 (see Section 5.3.4). Thus, we surmise that the optomechanical back-action is caused by photothermal forces. Further details of the analysis are included below.

5.3.2 Photothermal Model

Here, we derive Equation 5.2. According to [56], the effective frequency ω_{eff} and damping Γ_{eff} should follow

$$\omega_{\mathrm{eff}}^2 = \omega_0^2 \left(1 - \frac{1}{1+\omega_0^2\tau^2}\frac{\nabla F}{K}\right) \tag{5.3}$$

$$\Gamma_{\mathrm{eff}} = \Gamma \left(1 + Q\frac{\omega_0\tau}{1+\omega_0^2\tau^2}\frac{\nabla F}{K}\right) \tag{5.4}$$

We are looking for $\nabla F_{\mathrm{pth}} = dF_{\mathrm{pth}}/dz$, where F_{pth} is the photothermal force felt by the membrane. We use the model illustrated in Fig. 5.5, in which a fully clamped circular graphene membrane with radius a and initial tension per unit length along the perimeter σ_0 is suspended a distance d away from a gate electrode. Let z

denote the vertical displacement of the center of the graphene membrane, and z_0 its equilibrium displacement from the flat membrane case due to an applied gate voltage. Our goal is to find the photothermal spring constant for small oscillations about $z = z_0$. We start by assuming that heating from the laser causes a tension change in the graphene proportional to the power of the electric field at position z:

$$\sigma_{pth} = AP \sin^2\left(\frac{2\pi}{\lambda}(d-z)\right) \tag{5.5}$$

where P is the incident laser power and λ is the laser wavelength. Assuming the tension arises from laser-induced heating, the proportionality constant A depends on many theoretical factors such as graphene's light absorption, thermal conductivity, and thermal expansion coefficient, but it can also be determined empirically (see Section 5.3.3). The external force that the contact exerts on the membrane is given by the z-component of the tension induced by the laser: $\nabla F_{\text{cont}} = -2\pi a \sigma_{pth} \sin\theta$, where θ is the contact angle (a function of z and gate voltage). The gradient is then

$$\nabla F_{\text{cont}} = -2\pi a(\sin\theta \nabla\sigma_{pth} + \sigma_{pth}\nabla\sin\theta)|_{z=z_0}$$

The first term is F_{pth} and has a time constant τ_{pth} associated with it, which depends on the thermal conductivity and specific heat capacity of graphene. The second term is related to the change in the contact angle as the membrane moves, which happens instantaneously and serves only to offset the mechanical spring constant K. Thus, the photothermal spring constant is given by

$$\nabla F_{pth} = AP\frac{4\pi^2 a}{\lambda}\sin(\theta_0) sin\left(\frac{4\pi}{\lambda}(d-z_0)\right) \tag{5.6}$$

where $\theta_0 = \theta(z_0)$. Note that $\nabla F_{pth} = 0$ when $\theta_0 = 0$, meaning that the membrane must start with a nonzero displacement in order to experience optomechanical effects. In other words, a gate voltage must be applied to the membrane to break

the symmetry; if the membrane were perfectly flat, the tension change due to the laser would act perpendicular to the degree of freedom and would not affect the motion. For the optomechanical system described in [46], this asymmetry condition is satisfied by making the resonator from two different materials to act as a bimetallic strip.

Next, we find θ_0 by exploring the equilibrium position of the membrane as a function of gate voltage. Assume that the shape of the membrane forms a spherical cap as it is pulled down by the electrostatic force from the gate [6]. The position of the center of the membrane is related to the contact angle by

$$z_0 = a\frac{1-\cos\theta_0}{\sin\theta_0} \tag{5.7}$$

The net external force on the membrane must be zero, so the upward force of the contact is equal to the downward force of the gate voltage. The total stress is $\sigma_{\text{tot}} = \sigma_0 + \frac{E}{1-\nu}\frac{\Delta L}{L} + \sigma_{\text{pth}}$ where σ_0 is the initial tension in the device in the absence of a gate voltage or laser, E is the 2D Youngs modulus (in N/m), ν is the Poisson ratio, and the strain $\frac{\Delta L}{L} = \frac{\theta_0}{\sin\theta_0} - 1$. The electrostatic force is given by $F_{gate} = \frac{1}{2}\frac{dC}{dz}V_g^2$, where C is the capacitance of the device. Assuming the membrane and the gate electrode form the two sides of a parallel plate capacitor, $\frac{dC}{dz} = \frac{\epsilon_0\pi a^2}{(d-z_0)^2}$. We arrive at an equation for the position of the membrane:

$$\frac{E}{1-\nu}\theta_0 - \sin\theta_0\left(\frac{E}{1-\nu} - \sigma_0 - AP\sin^2\left(\frac{2\pi}{\lambda}(d-z_0)\right)\right) = \frac{\epsilon_0 a V_g^2}{4(d-z_0)^2} \tag{5.8}$$

where z_0 is given by Eq. 5.7.

Expanding this equation to first order in θ_0 gives

$$\theta_0 = \frac{\epsilon_0 a d V_g^2}{4d^3(\sigma_0 + AP\sin^2(2\pi d/\lambda)) - \epsilon_0 a^2 V_g^2} \tag{5.9}$$

We can solve Eq. 5.9 numerically by using specific parameters from one of our devices, and we find that the first order approximation of θ_0 departs from the exact value quickly, at around $V_g = 5$ V for Device 2.

Note that when V_g is small, $\nabla F_{\rm pth} \propto P V_g^2$ (see Fig. 5.8). Hence, the observed optomechanical effects depend strongly on gate voltage. In addition, by using the gate voltage to pull the graphene membrane through a node in the optical field (Figure 5.4), we can cause $F_{\rm pth}$ to change sign, thereby enhancing or reducing the damping.

5.3.3 Finding Parameters

Determining A Experimentally

We use the frequency of the graphene as a function of laser power at low gate voltage to obtain an experimental measure of A for Device 2. The frequency of a circular drumhead resonator is given by

$$f = \frac{2.404}{2\pi a}\sqrt{\frac{\sigma}{\rho}}$$

where we assume $\sigma = \sigma_0 + \sigma_{\rm pth}$ is the stress in the resonator in the absence of gate voltage. In the limit of $\sigma_{\rm pth} \ll \sigma_0$, we can expand this to find:

$$f \approx \frac{2.404}{2\pi a}\sqrt{\frac{\sigma_0}{\rho}}\left(1 + \frac{\sigma_{pth}}{2\sigma_0}\right) \tag{5.10}$$

In order to get an estimate for A, we measure the frequency versus laser power at a gate voltage ($V_g = 0.8$ V) that is too low to significantly affect the tension or cavity length, but high enough to make the device resonate at a detectable amplitude. Fitting Eq. 5.10 and Eq. 5.5 to the data in Fig. 5.6 yields $f_0 = \frac{2.404}{2\pi a}\sqrt{\frac{\sigma_0}{\rho}} = 5.042 \pm .005$ MHz and $A = 15$ N/(m $\cdot$ W) using the values from Section 5.1.2.

We can also estimate A from thermal expansion. Assuming pure thermal expansion in a circular membrane and absorption $\pi\alpha$ from Ref. [113] (see also Appendix A), we find that in the cavity $A = -2\alpha E \alpha_g / t\kappa(1-\nu) = 4$ N/(m$\cdot$W), where α is the fine structure constant, $\kappa = 5000$ W/(m $\cdot$ K) is the thermal conductivity κ, $E \approx 60$

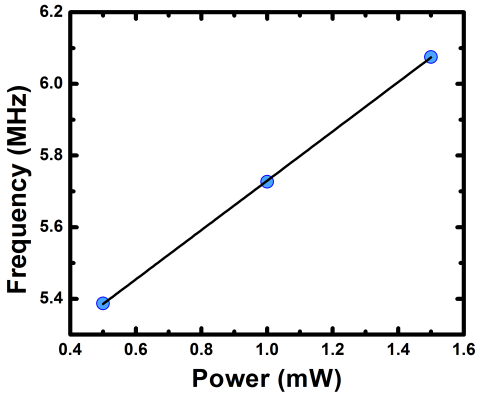

Figure 5.6: Frequency of Device 2 at $V_g = 0.8$ V as a function of laser power.

N/m is the Young's modulus of CVD graphene [107], $t = 0.335$ nm is the thickness of graphene, $\alpha_g \approx -7 \times 10^{-6}$ is the thermal expansion coefficient of graphene [140] , and $\nu = 0.16$ is the Poisson ratio for graphene. This value is in reasonable agreement with the experimentally determined value of $A = 15$ (N/m·W) considering the assumptions and the uncertainty in the theoretical numbers, especially Youngs modulus [107].

Estimating τ

In order to compare the size of the observed optomechanical effect to that predicted by Eq. 5.4 and 5.6, we must estimate τ. Assuming a circular membrane resonator, the thermal equilibration time constant can be approximated as $\tau = a^2 \rho C / 2\kappa$, where $C = 700$ J/(kg·K) is the specific heat of the graphene and $\kappa = 5000$ W/(m·K) is the thermal conductivity. For the circular membrane resonator observed here, $\tau = 5$ ns.

5.3.4 Testing The Theory

Estimating Photon-Induced Rigidity

We can compare these values to the experimentally obtained values for Device 2 in Fig. 5.4. The slope of Fig. 5.4d together with Eq. 5.4 yields an experimental value of $\frac{d\nabla F}{dP} = 0.7$ N/(m·W). The value predicted by Eq. 5.6, using Eq. 5.9 to find θ_0, is = 4.4 N/(m·W). For Fig. 3c, the experimental number is $\frac{d\nabla F}{dP} = -17$ N/(m·W), while the theoretical estimate is $\frac{d\nabla F}{dP} = -202$ N/(m·W), where this time Eq. 5.8 must be solved to find θ_0. This agreement is reasonable considering the important dependence on θ_0 and z_0, which must be estimated theoretically, and the approximations involved in our model (we ignore the curvature of the membrane in the light field and the finite laser spot size).

λ Dependence

The above theory for photothermal optomechanical coupling makes several predictions that can be tested experimentally. First, the optomechanical damping Γ_{OM} should depend sinusoidally on laser wavelength. We use a tunable-wavelength Ti:Sapphire laser to test this hypothesis on Device 2 from $\lambda = 700$ nm to $\lambda = 840$ nm. Figure 5.7 shows that the theory (Eq. 5.4 and 5.6) predicts the damping accurately over this range. To fit the frequency, we use a modified version of Eq. 5.3 that takes into account both static absorption-induced stress and optomechanical back-action:

$$\omega_{\mathrm{eff}}^2 = \omega_0^2 \left(1 + B \sin^2\left(\frac{2\pi}{\lambda}(d-z)\right) - \frac{C}{\lambda}\sin\left(\frac{4\pi}{\lambda}(d-z)\right)\right) \tag{5.11}$$

where B and C are proportionality constants. This modified version captures the trend in the data. We note that according to the theory, $B = AP/\sigma$ (Eqs. 5.5 and 5.10), and $C = 4\pi^2 aAP\sin(\theta_0)K^{-1}(1+\omega_0^2\tau^2)^{-1}$ (Eq. 5.6). If we leave B, C,

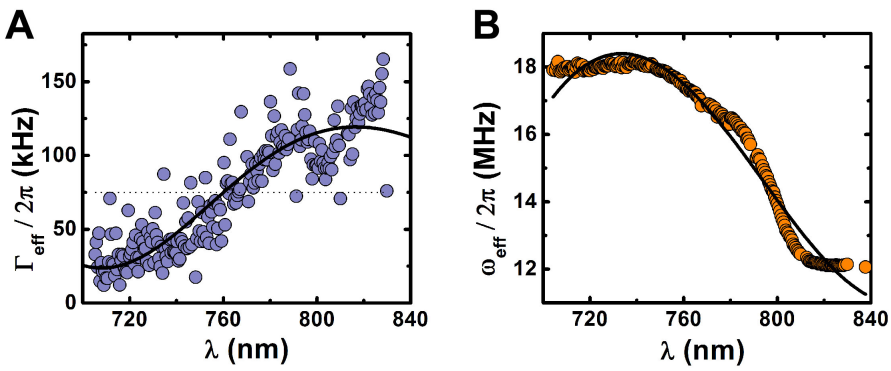

Figure 5.7: (a) Damping of Device 2 at $V_g = 16$ V, $P = 3$ mW as a function of wavelength. The dotted line indicates the intrinsic damping measured at low laser power. The black line is a fit to Eq. 5.4 with $d - z = 1330$ nm (measured at $V_g = 16$ V from where $dR(\lambda)/dz = 0$). (b) Frequency as a function of wavelength for the same measurement. The black line is a fit to Eq. 5.11 with $d - z = 1330$ nm.

and ω_0 as fit parameters, we find $B = 1.13$, $C = 400$ nm, and $\omega_0/2\pi = 12$ MHz. These numbers agree well with the theoretical values of $B = 0.71$ and $C = 800$ nm, where we have used $\sigma = (\omega_0/2.404)^2 a^2 \rho = 0.064$ N/m to find B theoretically.

It is worth mentioning that comparing the optomechanically-induced frequency shift (as given by C) to the damping shift in Figure 5.7a gives an independent measurement of $\omega_0\tau$. Interestingly, we find by this method that $\omega_0\tau = 0.008$, which gives $\tau = 0.1$ ns, a much lower value than the estimate of $\tau = 5$ ns in section 5.3.3. This estimate should be taken with a grain of salt because of the the three-parameter fit in Figure 5.7B, but it necessitates further investigation into the time constant governing the optical feedback in these systems.

V_g Dependence

Equation S-4 also predicts a dependence of the optomechanical damping on gate voltage, since θ_0 is a function of V_g. For small V_g and P, we find that $\theta_0 \propto V_g^2$,

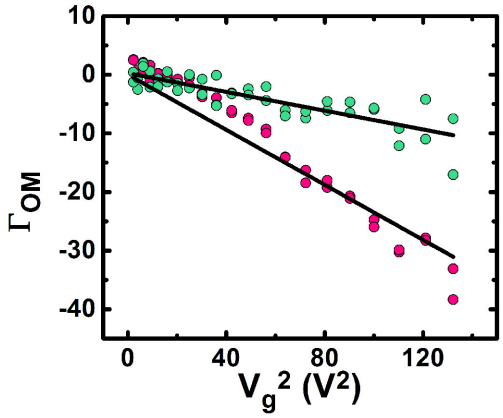

Figure 5.8: Optomechanically induced damping Γ_{OM} for Device 1 at a given laser power (shown for 0.3 mW, green; and 2 mW, pink) depends on gate voltage roughly as V_g^2. We determine $\Gamma_{OM} = \Gamma_{eff} - \Gamma$ by assuming the intrinsic damping Γ can be measured at low laser power. We use $\Gamma = \Gamma_{\text{eff}}(P = 100\mu\text{W})$. Black lines are linear fits to the data with a y-intercept of $\Gamma_{OM}(V_g = 0) = 0$.

and therefore $\theta_0\Gamma_{OM} \propto PV_g^2$. Figure 5.8 shows the measured optomechanically-induced damping as a function of V_g^2 for two different laser powers, which agrees well with this prediction.

5.3.5 Radiation Pressure

We also consider the possibility of an optomechanical effect from radiation pressure. According to Ref. [56], the maximal force gradient due to radiation pressure is:

$$\nabla F_{rad} = \frac{2P}{c\lambda} 2\sqrt{R_g} g^2 \tag{5.12}$$

where $g^2 = 4R/(1-R)^2$ is the coefficient of finesse, $R = (R_g R_e)^{1/2}$, R_g is the reflectance of the graphene, and $R_e \approx 1$ is the reflectance of the platinum electrode. Using $R_g \approx \pi^2\alpha^2(1-\pi\alpha)/4 = 1.3 \times 10^{-4}$, at $P = 5$ mW and $\lambda = 633$ nm, we find $\nabla F_{rad} \approx 5 \times 10^{-7}$ N/m, which is too small compared to the resonator spring constant $K = 0.1$ N/m to be of significance.

5.4 Self Oscillation and Cooling

5.4.1 Self-Oscillation

When the damping from the light field Γ_{OM} is negative, sufficiently high laser powers will cause regenerative self-oscillation in the graphene membrane [44, 59]. Figure 5.9 shows the amplitude of oscillation of Device 1 as a function of CW laser power with a DC gate voltage $V_g = -12$ V applied. No time-varying drive force is applied to the graphene. At low laser powers, the graphene vibrates due to Brownian motion. As laser power is increased, the amplitude of motion increases rapidly, demonstrating regenerative self-oscillation. Like the driven oscillation, the self-oscillation of the membrane can be tuned in frequency. Figure 5.9b shows the self-oscillation of Device 2, which can be tuned in frequency from 11 MHz to 17 MHz as gate voltage is changed from $V_g = -16$ V to $V_g = -20$ V. Tunable-frequency self-oscillation of a graphene membrane is useful for applications in photonics and signal processing [42]. In Fig. 5.9b, the graphene acts as a frequency-tunable modulator of light requiring only a gate voltage to adjust its resonant frequency.

Injection locking behavior

Of further interest is injection locking behavior [60], demonstrated here using both electrical and optical pilot signals. This behavior could be used to synchronize two optomechanical resonators via electrical or optical signals, or for all-optical amplification.

When the graphene is self-oscillating and a small electrical drive signal is applied, the graphene membrane motion locks to the drive signal (Fig. 5.10). The jump in frequency near $V_g = 5$ V appears only at high laser power and is likely related to previously observed interactions between the photothermal force and

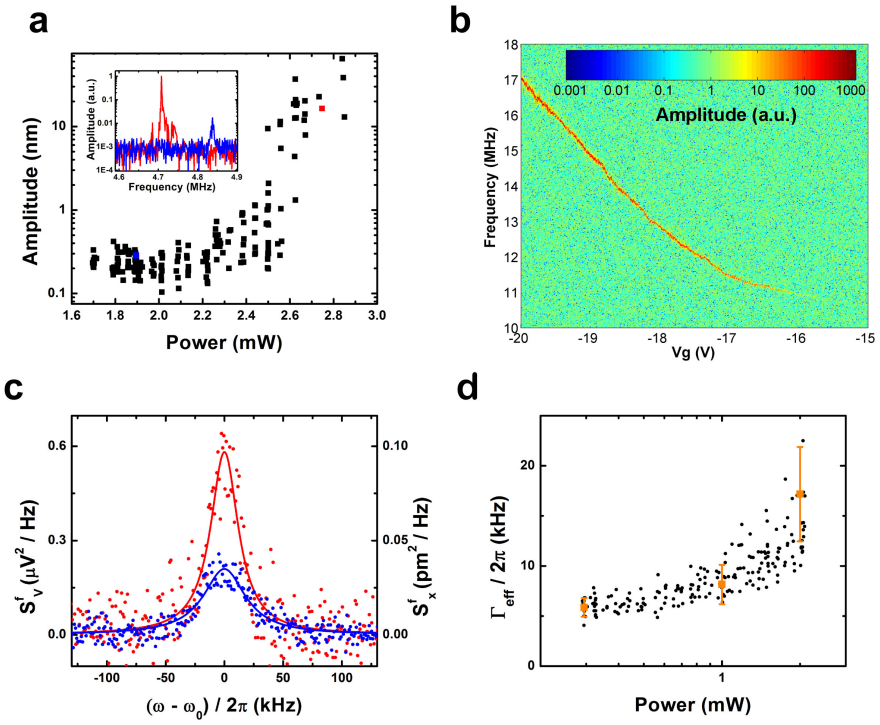

Figure 5.9: Optomechanically induced self-oscillation and cooling for Device 2 (b only) and Device 1 (all other figures). Data in (a-c) was acquired by applying only a continuous wave laser and a DC gate voltage to the devices. (a) Amplitude of oscillation as a function of CW laser power, with $V_g = -12$ V, $\lambda = 633$ nm. The reflectance amplitude is calibrated to displacement using the thermal motion at low powers [4]. Inset: examples of log-scale amplitude of oscillation versus frequency for two different laser powers: 1.9 mW (blue) and 2.6 mW (red). The dramatic increase in amplitude for the small increase in laser power is evidence of self oscillation. (b) Log-scale amplitude versus frequency and gate voltage at $\lambda = 532$ nm, $P = 1.5$ mW, showing that the frequency can be tuned as the device is self-oscillating. (c) Laser cooling of a graphene membrane at $\lambda = 718$ nm. Brownian noise spectra shown for laser powers of 1 mW (red) and 2 mW (blue) are calibrated using the method from [4]. At the higher laser power, the area under the curve diminishes by a factor of two, demonstrating that the membrane has been cooled. (d) Width of the driven peak versus laser power at $\lambda = 718$ nm (black); measurements at specific powers (orange) are used to estimate the expected temperature of the undriven peaks in (c).

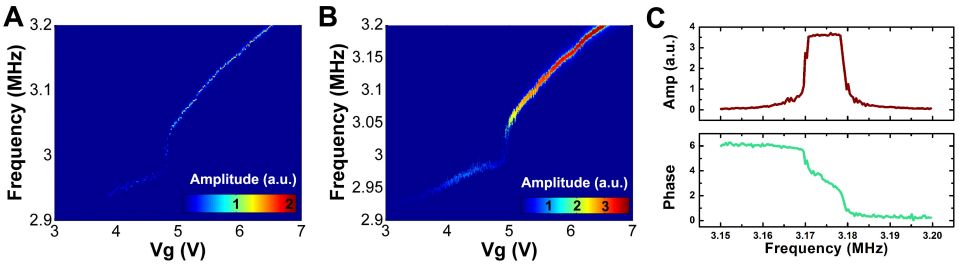

Figure 5.10: Injection locking behavior in Device 1. (A) No drive; the self-oscillation frequency of the device tunes with gate voltage. (B) An electrical driving force (-60 dBm) is applied between the gate and the drain. (C) Amplitude and phase versus frequency at $V_g = 6.17$ V from the data in (B).

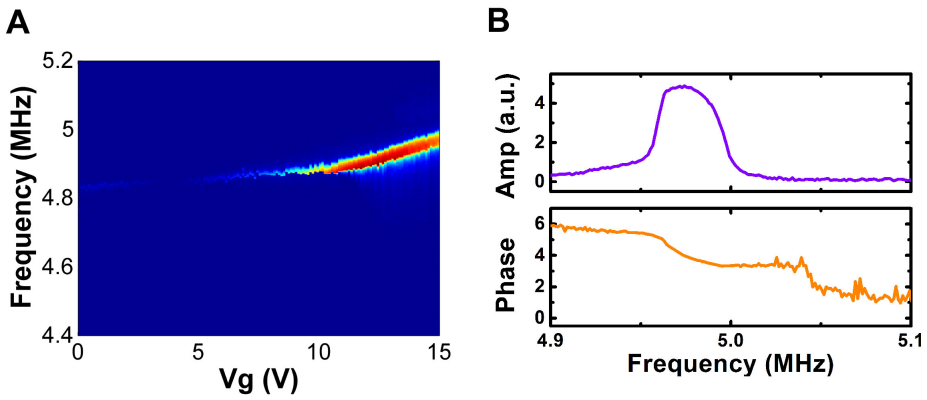

Figure 5.11: Locking to an optical signal in Device 1. (A) An optically modulated signal ($\lambda = 405$ nm, $P = 1.8$ mW) is used to drive the graphene motion; a red laser ($\lambda = 633$ nm, $P = 2$ mW) is used to read the motion. The reflected light is filtered so that only the $\lambda = 633$ nm light is detected by the photodiode. For $V_g > 10$ V, the graphene exhibits self-oscillation and locks to the drive signal. (B) Amplitude and phase versus frequency at $V_g = 15$ V from the data in (A).

the electrical force governing the length of the cavity [45].

We also observe injection locking to a modulated optical signal, with no modulated voltage applied to the graphene (Fig. 5.11). These phenomena could be useful for microwave photonics if optomechanical coupling can be demonstrated in graphene resonators with frequencies in the microwave range.

5.4.2 Laser Cooling

When Γ_{OM} is positive, the laser can be used to cool the thermal motion of the membrane. At $\lambda = 718$ nm, the area under the Device 1 Brownian motion peak decreases by about a factor of 2 when laser power increases from 1 mW to 2 mW (Fig. 5.9c). We calculate the effective temperature T_{eff} by noting that the width of the driven motion is also inversely proportional to temperature [56]:

$$\frac{T_{\mathrm{eff}}}{T} = \frac{\Gamma}{\Gamma_{\mathrm{eff}}} \tag{5.13}$$

where T and Γ are the temperature and damping at low laser power. The width Γ_{eff} of the driven motion as a function of power is shown in Fig. 5.9d. According to Eq. 5.13, the temperature at $P = 1$ mW is 210 ± 60 K, and the temperature at $P = 2$ mW is 100 ± 40 K. These temperatures are consistent with the change in area under the Brownian motion peaks. We note that the laser-induced heating of the graphene at $P = 2$ mW is less than $\Delta T \approx 20$ K at the detuning for maximum possible absorption.

5.5 Miscellaneous Applications

We consider the possibility of using graphene optomechanical resonators for room temperature applications in force and position sensing. The ability to resolve the thermal motion of graphene indicates a position sensitivity of $600\mathrm{fm/Hz}^{1/2}$ for

the membrane laser-cooled to 100 K. This sensitivity is limited by noise from the photodetector and corresponds to a force sensitivity of 300aN/Hz$^{1/2}$, the highest experimentally achieved for graphene to date and comparable to that of state-of-the-art silicon cantilevers at room temperature [157] but with a much smaller device footprint. It could be further improved by cryogenic cooling and taking advantage of optomechanical effects [40], or by incorporating the graphene membrane into a high-finesse cavity [147].

5.6 Photothermal Cooling

5.6.1 Broad Limitations from Quality Factor

We also consider the application of graphene resonators to future experiments in quantum mechanics. First, we evaluate the minimum possible temperature that can be reached with laser cooling via the photothermal effect [56]:

$$\frac{T_{\text{eff,min}}}{T} = \frac{1}{1 + Q/2} \tag{5.14}$$

which yields $T_{\text{eff,min}} = 700$ mK when applied to the room-temperature device in Fig. 4. This is not sufficient to reach the quantum ground state of the resonator at $T_Q = \hbar\omega/k_B = 0.2$ mK from room temperature. However, the graphene resonator studied in Ref. [9] has a resonant frequency of 75 MHz and Q = 9000 at 9 K, from which photothermal cooling to the quantum ground state is possible according to Eq. 5.14.

5.6.2 Limitations from Strength of ∇F

Although there is no fundamental limitation that would prevent cooling to the ground state by a photothermal effect [54, 55], it is challenging because the cooling

effect must be strong enough to compensate for the heating due to absorbed laser power. We analyze these competing effects in below and conclude that the strength of the cooling effect observed here is large enough to cool the aforementioned 75 MHz resonator from 9K to the quantum ground state, assuming it could be engineered such that $\omega_0\tau = 1$.

First, we note that the effective temperature T_{eff} reached using laser cooling from a bath temperature T is given by Eq. 5.4

$$\frac{T_{\text{eff}}}{T} = \frac{1}{1 + Q\frac{\omega_0\tau}{1+\omega^2\tau^2\frac{\nabla F}{K}}} \tag{5.15}$$

We assume $\omega_0\tau = 1$. The photon-induced rigidity for arbitrary cavity detuning $\phi_0 = \frac{4\pi}{\lambda}(d - z_0)$ is $\nabla F = \eta \sin(\phi_0) P$, where $\eta = (4\pi^2 a/\lambda) A \sin\theta_0$ denotes the linear power dependence of ∇F. In this work, we measured $\eta \sin(\phi_0) = -17$ N/(m$\cdot$ W) for Device 2 at $V_g = -10$V. To obtain a conservative estimate of the size of the effect, we will assume that this is the value measured at optimal cavity detuning $\sin(\phi_0) = -1$, so that $\eta = 17$ N/(m$\cdot$ W). Thus we have:

$$\frac{T}{T_{\text{eff}}} = \frac{\Gamma_{\text{eff}}}{\Gamma} = 1 + \frac{Q}{2}\frac{\eta \sin(\phi_0)}{K} P \tag{5.16}$$

The minimum T_{eff} is limited by the fact that the laser causes heating of the membrane as it is cooling the mechanical motion. To account for this effect, when the heating power of the laser causes a temperature rise ΔT, we must replace the base temperature T with $T + \Delta T$. Following Ref. [56], the absorbed laser power P_a causes a temperature rise $\Delta T = \beta P_a$, where β is a proportionality constant given here by $\beta = (2\pi t\kappa)^{-1}$. From Appendix A, $P_a = 4\pi\alpha \sin^2(2\pi d/\lambda) P$. Thus we have:

$$\frac{T + \Delta T}{T_{\text{eff}}} = \frac{T + 4\pi\alpha\beta \sin^2(\phi_0/2) P}{T_{\text{eff}}} = 1 + \frac{Q}{2}\frac{\eta \sin(\phi_0)}{K} P \tag{5.17}$$

$$T_{\text{eff}} = \left(T + 4\pi\alpha\beta \sin^2(\phi_0/2)P\right) / \left(1 + \frac{Q}{2}\frac{\eta \sin(\phi_0)}{K}P\right) \tag{5.18}$$

As an example, we will use the resonator from [9], which had $\omega_0 = 2\pi \times 75$ MHz and $Q = 9000$ at a temperature of $T = 9$K. Taking a typical $K = 0.1$ N/m and a detuning of $\phi_0 = \pi/10$, $P = 15$ mW leads to an effective temperature $T_{\text{eff}} = 3.4$ mK, comparable to the ground state temperature of $T_Q = 3.6$ mW while satisfying the stability condition $\nabla F/K < 1$.

Note that Eq. 5.18 implies that there is an advantage to detuning the cavity toward the point of minimal absorption, which increases the size of the optomechanical effect relative to the amount of absorbed laser power limiting P_{max}. The ability to detune the cavity with gate voltage is a crucial advantage in this respect.

This result is surprising, but attributable to the fact that the observed photothermal effect is relatively large given the low cavity finesse. In Fig. 5.4 we estimate 0.01 N/m at 500 μW, compared to 0.001 N/m at 130μW in Ref. [46]. We note that the optomechanical effect observed here is different in two major ways from previously observed bimetallic expansion effects in metal-coated cantilevers [46]. First, fully clamped graphene membranes can utilize their intrinsic tension for optomechanical feedback, whereas cantilevers have no such tension. Second, graphene has unusually high thermal conductivity [158], which here enables feedback at nanosecond timescales and could allow scaling of graphene optomechanics into the GHz regime.

5.7 Outlook

We have demonstrated photothermal back-action coupling to a graphene membrane, with potential applications in photonic signal processing and quantum electromechanical systems. The ultimate limits of laser cooling by this technique

require testing at low base temperatures, where quality factor will improve and thermal transport properties of graphene will differ. It is also important to note that for other areas of optomechanics that can benefit from low-mass membranes, such as coupling to clouds of laser-cooled atoms, radiation pressure coupling would be ideal [159]. For this reason, investigation of alternative means of achieving optomechanical coupling to graphene and other two-dimensional materials is needed. However, as a means of achieving optomechanical coupling to graphene, the technique described here has the advantage that the devices are simple to fabricate and the effect is powerful without a high-finesse cavity, obviating the need for further engineering. Compared to other materials that have been used for photothermal optomechanics, graphene resonators offer the advantages of strong mechanical frequency tunability and an extremely low mass that enhances their frequency-to-stiffness ratio. In general, graphene optomechanical systems provide a way to strongly couple mechanical, optical, and electrical degrees of freedom within a single material, which will enable experimentation in mechanical nonlinear dynamics.

Chapter 6

Conclusions and Outlook

This dissertation has focused on mechanical devices made from graphene. We believe that the techniques developed here for engineering large scale arrays of graphene NEMS with good mechanical properties will be useful for a wide variety of applications, of which only a small subset are explored here. In identifying the unique advantages of two-dimensional graphene nanoelectromechanical systems, it is helpful to consider the properties of a closely related system: one-dimensional NEMS. For example, carbon nanotubes have ultra-low mass and reasonably high quality factor, which makes them useful for mass sensing (Eq. 1.8). Indeed, carbon nanotube mass sensors have already achieved single-proton resolution [28], which would be difficult for graphene to match. However, graphene's large area offers a different set of opportunities.

6.1 Prospects for Graphene Optomechanics

Ultimately, the distinguishing feature of graphene NEMS is their extremely low mass to area ratio. Thus, they are most beneficial in applications where both low mass and high area are required. Optomechanics is a good example – graphene optomechanical systems have a low mass that decreases their stiffness $K = m\omega^2$ and enhances their zero point motion $x_{zp} = \hbar\omega/2K$, while their large area makes them simple to couple to optical fields and innately compatible with nanofabrication techniques. The combination of these properties makes graphene resonators unlike any system previously used for photothermal optomechanics. In particular, the high frequency to stiffness ratio brings the ground state within reach while keeping the devices soft enough to respond to photothermal forces, making these

devices (to our knowledge) the first for which ground state cooling seems achievable using the photothermal effect. Other methods of optomechanical coupling can also utilize graphene's large area. In particular, capacitive coupling will be useful for both cavity detection of the motion [149] and cooling to the quantum ground state [51].

However, before moving toward applications of graphene optomechanics, there are important fundamental investigations that should be done to better understand the effect. There are two major pieces of the photothermal optomechanics picture that remain poorly understood after this preliminary work. The first is the laser-induced frequency shift, which appeared to be reasonably well reproduced by the model in Section 5.3.4 but which also shows some properties that we have not endeavored to explain. For example, in Figure 5.4A-B, there is a 'kink' in the frequency as a function of gate voltage around $V_g = -7$ V. The second factor is the photothermal time constant, τ. Our rough experimental measurement of τ yielded a value about 50 times smaller than the predicted value. This is surprising and deserves further investigation. One simple way to investigate τ would be to examine the size dependence of Γ_{OM}, since $\tau \sim a^2$. Another would be to utilize the dynamic methods found in [46].

In thinking about the future of graphene optomechanics, it is also worth thinking about the size dependence of the effect. Making the devices smaller will boost their frequency, bringing them closer to the GHz regime and making them more relevant for applications. However, the photothermal force described here gets dramatically weaker at smaller device sizes. From Eq. 5.4 and 5.2, the size-dependent factors in the strength of Γ_{OM}/Γ are $Q\omega_0\tau a\theta_0$, which gives $\Gamma_{OM}/\Gamma \sim a^4$. This analysis shows that optomechanical back-action will be difficult to achieve in small graphene devices, but it also provides a strong motivation to investigate the low-

temperature behavior of this effect, since lowering the temperature will increase τ by lowering the thermal conductivity and improve Q and ω_0 as has been shown previously.

For this reason and many others, repeating the optomechanics experiments at lower temperatures is the clear next step for this work. In addition to improving the magnitude of optomechanical effects in even small devices and bring graphene much closer to the quantum ground state, low-temperature graphene optomechanics could provide new physical mechanisms for photothermal optomechanics. For example, in graphene at low temperatures hot electrons require hundreds of picoseconds to equilibrate with the lattice [152, 160], long enough to make this delay relevant for photothermal effects. Alternate methods of achieving the delay necessary for optomechanical feedback are important because they decouple τ from device size and enable experimentation with smaller, high-frequency devices.

In terms of applications, graphene optomechanics may have other uses besides cooling toward the quantum ground state. For example, optomechanics has been used to enhance the force sensitivity of resonant structures. The analysis in [45] suggests that the force sensitivity of graphene could be enhanced by more than an order of magnitude by using optomechanics to artificially lower its spring constant. For photonic signal processing, graphene has significant advantages in its tunable frequency and its ability to exhibit optomechanical back-action at a wide range of wavelengths. For example, a signal transmitted by light modulated at an RF-carrier frequency could be mixed down to the baseband simply by reflecting from a graphene optomechanical system like those described here. The power of the optical beam would induce self-oscillation in the optomechanical system, while mixing between the mechanical frequency of the device and the RF carrier frequency would accomplish the down-conversion of the signal [42]. The disadvantage of graphene

optomechanical systems - low optical quality factor - might be alleviated by incorporating the graphene into a higher-finesse cavity [147], while graphene has the great advantage of a highly tunable mechanical frequency that would enable selective down-conversion. To name another application, the observation of injection locking [60, 61] in these systems paves the way for both electrically- and optically-induced synchronization between two graphene optomechanical systems [161, 162].

Finally, there may be important applications for other 2D materials in optomechanics, particularly where low-mass membranes are preferred. For example, for radiation-pressure coupling to clouds of laser-cooled atoms [159], the coupling constant is $g = \frac{\omega_{at}}{2}\sqrt{\frac{Nm\omega_{at}}{M\omega_m}}$, where ω_{at} is the atomic frequency, m is the atomic mass, N is the number of atoms, M is the resonator mass, and ω_m is the resonator frequency. Replacing the 50-nm thick nitride membranes of [159] with, e.g., monolayer BN would yield an improvement of at least an order of magnitude in the coupling coefficient while maintaining low absorption (careful studies of light absorption in BN should be conducted to confirm this point). In general, the low mass of atomically thin membranes ought to give them the same mechanical advantages associated with graphene but with different optical and electrical properties. In addition to dielectrics like BN, semiconducting monolayers like MoS_2 could be useful because they may allow new means of optomechanical coupling [156] beyond radiation pressure and photothermal forces.

6.2 Prospects for Graphene Force Sensors

We have seen that graphene is extraordinarily sensitive to forces, with experimentally demonstrated sensitivities comparable to those of silicon cantilevers at room temperature and the possibility of optomechanical sensitivity enhancement. Be-

cause the resonators we have demonstrated have a much smaller footprint than typical silicon cantilevers, however, this leaves the possibility of using an array of many graphene resonators as a force sensor; their measurements could be averaged to improve overall sensitivity. Perhaps more importantly, as a result of their high frequency-to-stiffness ratio, graphene resonators have a much higher bandwidth than traditional cantilever force sensors, which operate with resonant frequencies in the kilohertz range. Graphene force sensors could be especially useful for electrometry [4] or magnetic resonance force microscopy [58].

For all of these applications, it is helpful to boost the quality factor of graphene resonators. In Chapter 3, we discussed methods of improving the room temperature quality factor of graphene by improving the resonator geometry and boundary conditions. In Chapter 4 we presented evidence that the Q could be further improved by increasing strain.

6.3 Final Words

The field of nanomechanics has been pushing miniaturization for more than a decade, and with graphene and other 2D materials, it is finally reaching the limits of thinness. Graphene resonators have already proven that they can be manufactured in large arrays. They resonate with predictable frequencies, quality factors in the thousands at room temperature, and good dynamic range; they can also be applied as sensors of mass or force or as optomechanical systems. We hope that in the coming years this new class of mechanical resonators will continue to enable new applications and experiments.

Appendix A

Derivation of Graphene Absorption in a Cavity

The amount of energy the graphene absorbs from the spatially varying electric field can be calculated from the interaction between light and Dirac fermions, and is proportional to the magnitude of the electric field squared: $W_a = \pi\alpha c\epsilon_0|E|^2$, where c is the speed of light, and ϵ_0 is the permittivity of free space [113]. Because the reflection coefficient of graphene is small ($r_g \sim 0.01$), we can assume that the total electric field is mostly determined by the sum of a single incident plane wave moving toward the back plane, and a single reflected plane wave moving away from it. The result is $|E|^2 = 4|E_0|^2 \sin^2(2\pi d/\lambda)$, where E_0 is the complex amplitude of the incoming plane wave. The factor of 4 comes from the fact that the incident and reflected waves combine constructively, doubling the amplitude of the electric field. We normalize W_a by the energy flux of the incident plane wave, $W_i = c\epsilon_0|E_0|^2$, to get the absorption as a function of position:

$$W_a/W_i = 4\pi\alpha \sin^2(2\pi d/\lambda) \tag{A.1}$$

Equation A.1 is also plotted in Fig. 5.3c.

Appendix B

Frequency vs Gate Voltage

We are able to infer the mass and initial tension of the resonators by fitting a tensioned membrane model to the frequency versus gate voltage data, taken at low laser power such that optomechanical effects are negligible. We apply the theory in Ref. [6] to a fully clamped 2D membrane in the shape of a spherical cap. Let S be the radius of curvature of the spherical cap. Equating the force from the contact to the electrostatic force from the gate gives the total tension: $\sigma = \frac{S}{2\pi a^2} F_{gate}$. The additional tension induced by stretching is $\sigma - \sigma_0 = \frac{E}{1-\nu}\frac{\Delta L}{L} \approx \frac{E}{1-\nu}\frac{a^2}{6S^2}$, assuming the strain $\Delta L/L$ is small. Combining these equations to eliminate S gives a cubic equation for the tension:

$$\sigma^2(\sigma - \sigma_0) = \frac{E}{1-\nu}\frac{F_{\text{gate}}^2}{24\pi^2 a^2} \tag{B.1}$$

The frequency of a tensioned circular resonator is given by $f = \frac{2.404}{2\pi a}\sqrt{\frac{\sigma}{\rho}}$, where ρ is the 2D mass density. Assume the electrostatic force is that of a parallel plate capacitor: $F_{\text{gate}} = \epsilon_0 \pi a^2 V_g^2 / 2d^2$. Note that in the limit of low tension ($\sigma \approx \sigma_0$), Eq. B.1 suggests that f scales as V_g^2, while in the limit of high tension ($\sigma \gg \sigma_0$) it scales as $V_g^{2/3}$.

We fit the following model to our frequency versus gate voltage data, using a nonlinear least squares method:

$$(f^2 - c_3 V_g^2 - c_1)(f^2 - c_3 V_g^2)^2 = c_2 V_g^4 \tag{B.2}$$

where c_1, c_2, and c_3 are fitting parameters. In terms of the theory outlined above, $c_1 = \frac{2.404^2}{4\pi^2 a^2}\frac{\sigma_0}{\rho}$ and $c_2 = \frac{2.404^6 \epsilon_0^2}{6144\pi^6 a^4 d^4 \rho^3}\frac{E}{1-\nu}$. Hence, we can extract initial tension σ_0 and density ρ from these two parameters. We add in the parameter c_3 to represent an offset to the spring constant proportional to V_g^2, which matches our

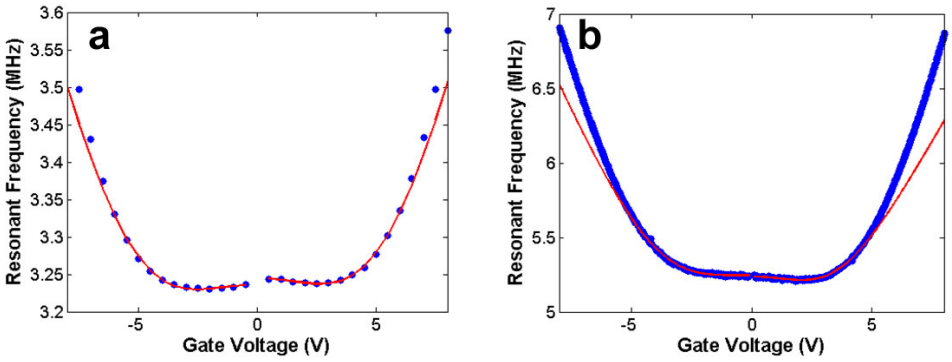

Figure B.1: Frequency versus gate voltage for Device 1 (a) and Device 2 (b). The blue dots are the data and the red lines are the fits. We only fit to $V_g^2 < 40V^2$ for Device 1, and $V_g^2 < 20V^2$ for Device 2. At higher gate voltages the tensioned membrane model diverges from the data.

data at low gate voltages. This term can arise from capacitive softening [116], however, if we use the density derived from c_2, we predict that c_3 should be much larger than what we observe. We suspect that there are other physical mechanisms that determine c_3, such as regions of initial slack [119]. The data and fits for Device 1 and Device 2 are plotted in Fig. B.1. The model fits well at low gate voltage and gives us reasonable values for σ_0 and ρ, but at high gate voltage the frequency continues to increase when the model's $V_g^{2/3}$ dependence rolls off. This is the subject of ongoing research.

BIBLIOGRAPHY

[1] I. Favero and K. Karrai, Nature Photonics **3**, 201 (2009).

[2] A. K. Geim, Science **324**, 1530 (2009).

[3] S. Bae et al., Nature Nanotechnology **5**, 574 (2010).

[4] J. S. Bunch et al., Science **315**, 490 (2007).

[5] J. S. Bunch et al., Nano Letters **8**, 2458 (2008).

[6] C. Y. Chen et al., Nature Nanotechnology **4**, 861 (2009).

[7] S. Shivaraman et al., Nano Letters **9**, 3100 (2009).

[8] J. T. Robinson et al., Nano Letters **8**, 3441 (2008).

[9] A. M. van der Zande et al., Nano Letters **10**, 4869 (2010).

[10] X. Liu et al., Journal of Applied Physics **97** (2005).

[11] J. Liu et al., Applied Physics Letters **99** (2011).

[12] S. S. Verbridge, D. F. Shapiro, H. G. Craighead, and J. M. Parpia, Nano Letters **7**, 1728 (2007).

[13] D. J. Wilson, C. A. Regal, S. B. Papp, and H. J. Kimble, Physical Review Letters **103** (2009).

[14] V. P. Adiga et al., Journal of Applied Physics **(In press)** (2012).

[15] R. A. Barton et al., Nano Letters **11**, 1232 (2011).

[16] R. R. Schaller, Ieee Spectrum **34**, 52 (1997).

[17] S. E. Thompson and S. Parthasarathy, Materials Today **9**, 20 (2006).

[18] Y. Developpement, Mems for cell phones and tablets, 2012.

[19] V. Kaajakari, *Practical MEMS*, Small Gear Publishing, New York, NY, 2009.

[20] K. L. Ekinci, X. M. H. Huang, and M. L. Roukes, Applied Physics Letters **84**, 4469 (2004).

[21] B. Ilic, Y. Yang, and H. G. Craighead, Applied Physics Letters **85**, 2604 (2004).

[22] B. Ilic et al., Journal of Applied Physics **95**, 3694 (2004).

[23] B. Ilic et al., Nano Letters **5**, 925 (2005).

[24] Y. T. Yang, C. Callegari, X. L. Feng, K. L. Ekinci, and M. L. Roukes, Nano Letters **6**, 583 (2006).

[25] K. Jensen, K. Kim, and A. Zettl, Nature Nanotechnology **3**, 533 (2008).

[26] B. Lassagne, D. Garcia-Sanchez, A. Aguasca, and A. Bachtold, Nano Letters **8**, 3735 (2008).

[27] H. Y. Chiu, P. Hung, H. W. C. Postma, and M. Bockrath, Nano Letters **8**, 4342 (2008).

[28] J. Chaste et al., Nature Nanotechnology **7**, 301 (2012).

[29] H. J. Mamin and D. Rugar, Applied Physics Letters **79**, 3358 (2001).

[30] K. Y. Yasumura et al., Journal of Microelectromechanical Systems **9**, 117 (2000).

[31] M. Poot and H. S. J. van der Zant, Physics Reports-Review Section of Physics Letters **511**, 273 (2012).

[32] R. Blatt and D. Wineland, Nature **453**, 1008 (2008).

[33] M. Roukes, Physics World **14**, 25 (2001).

[34] A. D. Armour, M. P. Blencowe, and K. C. Schwab, Physical Review Letters **88** (2002).

[35] K. C. Schwab and M. L. Roukes, Physics Today **58**, 36 (2005).

[36] A. D. O'Connell et al., Nature **464**, 697 (2010).

[37] M. Aspelmeyer, Nature **464**, 685 (2010).

[38] T. J. Kippenberg and K. J. Vahala, Science **321**, 1172 (2008).

[39] T. Corbitt et al., Physical Review Letters **98** (2007).

[40] O. Arcizet, T. Briant, A. Heidmann, and M. Pinard, Physical Review A **73** (2006).

[41] M. Bagheri, M. Poot, M. Li, W. P. H. Pernice, and H. X. Tang, Nature Nanotechnology **6**, 726 (2011).

[42] M. Hossein-Zadeh and K. J. Vahala, Ieee Photonics Technology Letters **20**, 234 (2008).

[43] G. S. Wiederhecker, L. Chen, A. Gondarenko, and M. Lipson, Nature **462**, 633 (2009).

[44] M. Zalalutdinov et al., Applied Physics Letters **79**, 695 (2001).

[45] M. Vogel, C. Mooser, K. Karrai, and R. J. Warburton, Applied Physics Letters **83**, 1337 (2003).

[46] C. H. Metzger and K. Karrai, Nature **432**, 1002 (2004).

[47] O. Arcizet, P. F. Cohadon, T. Briant, M. Pinard, and A. Heidmann, Nature **444**, 71 (2006).

[48] A. Schliesser, P. Del'Haye, N. Nooshi, K. J. Vahala, and T. J. Kippenberg, Physical Review Letters **97** (2006).

[49] S. Gigan et al., Nature **444**, 67 (2006).

[50] D. Kleckner and D. Bouwmeester, Nature **444**, 75 (2006).

[51] J. D. Teufel et al., Nature **475**, 359 (2011).

[52] J. Chan et al., Nature **478**, 89 (2011).

[53] L. K. W. Regal, C. A., Journal of Physics Conference Series **264**, 012025 (2011).

[54] J. Restrepo, J. Gabelli, C. Ciuti, and I. Favero, Comptes Rendus Physique **12**, 860 (2011).

[55] S. De Liberato, N. Lambert, and F. Nori, Physical Review A **83** (2011).

[56] C. Metzger, I. Favero, A. Ortlieb, and K. Karrai, Physical Review B **78** (2008).

[57] M. D. LaHaye, O. Buu, B. Camarota, and K. C. Schwab, Science **304**, 74 (2004).

[58] D. Rugar, R. Budakian, H. J. Mamin, and B. W. Chui, Nature **430**, 329 (2004).

[59] T. J. Kippenberg, H. Rokhsari, T. Carmon, A. Scherer, and K. J. Vahala, Physical Review Letters **95** (2005).

[60] M. Zalalutdinov et al., Applied Physics Letters **83**, 3281 (2003).

[61] M. Hossein-Zadeh and K. J. Vahala, Applied Physics Letters **93** (2008).

[62] C. Metzger et al., Physical Review Letters **101** (2008).

[63] T. Carmon, M. C. Cross, and K. J. Vahala, Physical Review Letters **98** (2007).

[64] X. L. Feng, C. J. White, A. Hajimiri, and M. L. Roukes, Nature Nanotechnology **3**, 342 (2008).

[65] O. Arcizet et al., Physical Review Letters **97** (2006).

[66] A. Schliesser, O. Arcizet, R. Riviere, G. Anetsberger, and T. J. Kippenberg, Nature Physics **5**, 509 (2009).

[67] R. G. Knobel and A. N. Cleland, Nature **424**, 291 (2003).

[68] J. D. Teufel et al., Nature **471**, 204 (2011).

[69] E. Verhagen, S. Deleglise, S. Weis, A. Schliesser, and T. J. Kippenberg, Nature **482**, 63 (2012).

[70] A. K. Geim and K. S. Novoselov, Nature Materials **6**, 183 (2007).

[71] A. H. Castro Neto, F. Guinea, N. M. R. Peres, K. S. Novoselov, and A. K. Geim, Reviews of Modern Physics **81**, 109 (2009).

[72] K. I. Bolotin et al., Solid State Communications **146**, 351 (2008).

[73] F. Schedin et al., Nature Materials **6**, 652 (2007).

[74] K. S. Kim et al., Nature **457**, 706 (2009).

[75] Y. M. Lin et al., Nano Letters **9**, 422 (2009).

[76] Y. M. Lin et al., Science **327**, 662 (2010).

[77] K. M. Milaninia, M. A. Baldo, A. Reina, and J. Kong, Applied Physics Letters **95** (2009).

[78] H. W. C. Postma, Nano Letters **10**, 420 (2010).

[79] G. F. Schneider et al., Nano Letters **10**, 3163 (2010).

[80] C. A. Merchant et al., Nano Letters **10**, 2915 (2010).

[81] S. Garaj et al., Nature **467**, 190 (2010).

[82] J. C. Meyer, C. O. Girit, M. F. Crommie, and A. Zettl, Nature **454**, 319 (2008).

[83] R. Barton, J. Parpia, and H. G. Craighead, Journal of Vacuum Science and Technology B **29**, 050801 (2011).

[84] X. K. Lu, H. Huang, N. Nemchuk, and R. S. Ruoff, Applied Physics Letters **75**, 193 (1999).

[85] X. K. Lu, M. F. Yu, H. Huang, and R. S. Ruoff, Nanotechnology **10**, 269 (1999).

[86] J. S. Bunch, Y. Yaish, M. Brink, K. Bolotin, and P. L. McEuen, Nano Letters **5**, 287 (2005).

[87] Y. B. Zhang, J. P. Small, W. V. Pontius, and P. Kim, Applied Physics Letters **86** (2005).

[88] Y. B. Zhang, J. P. Small, M. E. S. Amori, and P. Kim, Physical Review Letters **94** (2005).

[89] K. S. Novoselov et al., Science **306**, 666 (2004).

[90] K. S. Novoselov et al., Proceedings of the National Academy of Sciences of the United States of America **102**, 10451 (2005).

[91] P. Blake et al., Applied Physics Letters **91** (2007).

[92] A. C. Ferrari et al., Physical Review Letters **97** (2006).

[93] A. Gupta, G. Chen, P. Joshi, S. Tadigadapa, and P. C. Eklund, Nano Letters **6**, 2667 (2006).

[94] C. Berger et al., Science **312**, 1191 (2006).

[95] K. V. Emtsev et al., Nature Materials **8**, 203 (2009).

[96] S. Stankovich et al., Nature **442**, 282 (2006).

[97] D. A. Dikin et al., Nature **448**, 457 (2007).

[98] G. Eda, G. Fanchini, and M. Chhowalla, Nature Nanotechnology **3**, 270 (2008).

[99] C. Gomez-Navarro, M. Burghard, and K. Kern, Nano Letters **8**, 2045 (2008).

[100] P. W. Sutter, J. I. Flege, and E. A. Sutter, Nature Materials **7**, 406 (2008).

[101] J. Coraux, A. T. N'Diaye, C. Busse, and T. Michely, Nano Letters **8**, 565 (2008).

[102] S. Y. Kim and H. S. Park, Nano Letters **9**, 969 (2009).

[103] A. Reina et al., Nano Letters **9**, 30 (2009).

[104] X. S. Li et al., Science **324**, 1312 (2009).

[105] P. Y. Huang et al., Nature **469**, 389 (2011).

[106] K. Kim et al., Acs Nano **5**, 2142 (2011).

[107] C. S. Ruiz-Vargas et al., Nano Letters **11**, 2259 (2011).

[108] X. S. Li et al., Journal of the American Chemical Society **133**, 2816 (2011).

[109] J. C. Meyer et al., Nature **446**, 60 (2007).

[110] K. I. Bolotin, F. Ghahari, M. D. Shulman, H. L. Stormer, and P. Kim, Nature **462**, 196 (2009).

[111] X. Du, I. Skachko, F. Duerr, A. Luican, and E. Y. Andrei, Nature **462**, 192 (2009).

[112] Y. H. Xu et al., Applied Physics Letters **97** (2010).

[113] R. R. Nair et al., Science **320**, 1308 (2008).

[114] L. Falkovsky, Journal of Physics: Conference Series **129**, 012004 (2003).

[115] K. L. Ekinci and M. L. Roukes, Review of Scientific Instruments **76** (2005).

[116] V. Singh et al., Nanotechnology **21** (2010).

[117] T. Mashoff et al., Nano Letters **10**, 461 (2010).

[118] D. Garcia-Sanchez et al., Nano Letters **8**, 1399 (2008).

[119] V. Sazonova et al., Nature **431**, 284 (2004).

[120] V. Gouttenoire et al., Small **6**, 1060 (2010).

[121] M. P. Levendorf, C. S. Ruiz-Vargas, S. Garg, and J. Park, Nano Letters **9**, 4479 (2009).

[122] B. Aleman et al., Acs Nano **4**, 4762 (2010).

[123] Y. X. Sun and M. Saka, Journal of Sound and Vibration **329**, 328 (2010).

[124] C. R. Dean et al., Nature Nanotechnology **5**, 722 (2010).

[125] X. S. Li et al., Nano Letters **9**, 4359 (2009).

[126] L. Y. Jiao et al., Journal of the American Chemical Society **130**, 12612 (2008).

[127] K. Jensen, J. Weldon, H. Garcia, and A. Zettl, Nano Letters **7**, 3508 (2007).

[128] A. K. Huttel et al., Nano Letters **9**, 2547 (2009).

[129] C. Seoanez, F. Guinea, and A. H. Castro, Physical Review B **76** (2007).

[130] S. Y. Kim and H. S. Park, Applied Physics Letters **94** (2009).

[131] H. Jiang, M. F. Yu, B. Liu, and Y. Huang, Physical Review Letters **93** (2004).

[132] J. Lischner and T. A. Arias, Physical Review B **81** (2010).

[133] T. S. Y. D. Weaver, W., Wiley: New York **9** (1990).

[134] I. Wilson-Rae et al., Physical Review Letters **106**, 4 (2011).

[135] S. S. Verbridge, J. M. Parpia, R. B. Reichenbach, L. M. Bellan, and H. G. Craighead, Journal of Applied Physics **99**, 8 (2006).

[136] Q. P. Unterreithmeier, T. Faust, and J. P. Kotthaus, Physical Review Letters **105** (2010).

[137] R. Aljishi and G. Dresselhaus, Physical Review B **26**, 4514 (1982).

[138] S. S. Verbridge, H. G. Craighead, and J. M. Parpia, Applied Physics Letters **92** (2008).

[139] C. Lee, X. D. Wei, J. W. Kysar, and J. Hone, Science **321**, 385 (2008).

[140] W. Z. Bao et al., Nature Nanotechnology **4**, 562 (2009).

[141] S. Scharfenberg et al., Applied Physics Letters **98** (2011).

[142] J. Kameoka, H. G. Craighead, H. W. Zhang, and J. Henion, Analytical Chemistry **73**, 1935 (2001).

[143] D. R. Southworth et al., Physical Review Letters **102** (2009).

[144] V. P. Adiga et al., Applied Physics Letters **99** (2011).

[145] N. Petrone et al., Nano Letters **12**, 2751 (2012).

[146] R. Barton et al., Nano Letters **ASAP** (2012).

[147] J. D. Thompson et al., Nature **452**, 72 (2008).

[148] G. Anetsberger et al., Nature Physics **5**, 909 (2009).

[149] X. F. Song et al., Nano Letters **12**, 198 (2012).

[150] A. Eichler et al., Nature Nanotechnology **6**, 339 (2011).

[151] F. Bonaccorso, Z. Sun, T. Hasan, and A. C. Ferrari, Nature Photonics **4**, 611 (2010).

[152] N. M. Gabor et al., Science **334**, 648 (2011).

[153] J. Yan et al., Nature Nanotechnology **7**, 472 (2012).

[154] X. K. Sun, J. J. Zheng, M. Poot, C. W. Wong, and H. X. Tang, Nano Letters **12**, 2299 (2012).

[155] R. Perahia, J. D. Cohen, S. Meenehan, T. P. M. Alegre, and O. Painter, Applied Physics Letters **97** (2010).

[156] K. Usami et al., Nature Physics **8**, 168 (2012).

[157] U. Gysin et al., Physical Review B **69** (2004).

[158] A. A. Balandin et al., Nano Letters **8**, 902 (2008).

[159] S. Camerer et al., Physical Review Letters **107** (2011).

[160] J. H. Strait et al., Nano Letters **11**, 4902 (2011).

[161] E. Buks and M. L. Roukes, Journal of Microelectromechanical Systems **11**, 802 (2002).

[162] M. Zhang et al., arXiv:1112.3636v2 (2012).